A&A 486, 177–189 (2008)
DOI: 10.1051/0004-6361:200809394
© ESO 2008

Astronomy & Astrophysics

The metal content of bulge field stars from FLAMES-GIRAFFE spectra

I. Stellar parameters and iron abundances⋆,⋆⋆

M. Zoccali[1], V. Hill[2], A. Lecureur[2,3], B. Barbuy[4], A. Renzini[5], D. Minniti[1], A. Gómez[2], and S. Ortolani[6]

[1] P. Universidad Católica de Chile, Departamento de Astronomía y Astrofísica, Casilla 306, Santiago 22, Chile
e-mail: [mzoccali;dante]@astro.puc.cl
[2] GEPI, Observatoire de Paris, CNRS, Université Paris Diderot; Place Jules Janssen, 92190 Meudon, France
e-mail: [Vanessa.Hill;Aurelie.Lecureur;Ana.Gomez]@obspm.fr
[3] Astronomisches Rechen-Institut, Zentrum für Astronomie der Universität Heidelberg, Mönchhofstr. 12−14, 69120 Heidelberg, Germany
[4] Universidade de São Paulo, IAG, Rua do Matão 1226, Cidade Universitária, São Paulo 05508-900, Brazil
e-mail: barbuy@astro.iag.usp.br
[5] INAF – Osservatorio Astronomico di Padova, Vicolo dell'Osservatorio 2, 35122 Padova, Italy
e-mail: alvio.renzini@oapd.inaf.it
[6] Università di Padova, Dipartimento di Astronomia, Vicolo dell'Osservatorio 5, 35122 Padova, Italy
e-mail: sergio.ortolani@unipd.it

Received 14 January 2008 / Accepted 26 April 2008

ABSTRACT

Aims. We determine the iron distribution function (IDF) for bulge field stars, in three different fields along the Galactic minor axis and at latitudes $b = -4°$, $b = -6°$, and $b = -12°$. A fourth field including NGC 6553 is also included in the discussion.
Methods. About 800 bulge field K giants were observed with the GIRAFFE spectrograph of FLAMES@VLT at spectral resolution $R \sim 20\,000$. Several of them were observed again with UVES at $R \sim 45\,000$ to insure the accuracy of the measurements. The LTE abundance analysis yielded stellar parameters and iron abundances that allowed us to construct an IDF for the bulge that, for the first time, is based on high-resolution spectroscopy for each individual star.
Results. The IDF derived here is centered on solar metallicity, and extends from [Fe/H] ∼ −1.5 to [Fe/H] ∼ +0.5. The distribution is asymmetric, with a sharper cutoff on the high-metallicity side, and it is narrower than previously measured. A variation in the mean metallicity along the bulge minor axis is clearly between $b = -4°$ and $b = -6°$ ([Fe/H] decreasing ∼ by 0.6 dex per kpc). The field at $b = -12°$ is consistent with the presence of a gradient, but its quantification is complicated by the higher disk/bulge fraction in this field.
Conclusions. Our findings support a scenario in which both infall and outflow were important during the bulge formation, and then suggest the presence of a radial gradient, which poses some challenges to the scenario in which the bulge would result solely from the vertical heating of the bar.

Key words. Galaxy: bulge – stars: abundances – stars: atmospheres

1. Introduction

The Galactic bulge is the nearest galactic spheroid, and it can be studied in greater detail than any other one. In particular, its stellar content can be characterized in terms of age and composition distribution functions, coupled with kinematical information. Thus, the bulge offers a unique opportunity to construct the star formation and mass assembly history of a galactic spheroid, hence providing a unique benchmark for theories of galaxy formation. The Galactic bulge is dominated by stellar populations older than ∼10 Gyr (Ortolani et al. 1995; Feltzing & Gilmore 2000; Zoccali et al. 2003), with no detectable trace of younger stellar populations. As a result, most of its stars were formed at a cosmic epoch that corresponds to $z \gtrsim 2$, making its study quite complementary to that of galaxies at such high redshifts.

Starting with the pioneering spectroscopic study of Rich (1988), the distribution function of the iron abundance among bulge stars has been further explored and refined by McWilliam & Rich (1994), Ibata & Gilmore (1995a,b) Minniti (1996), Sadler et al. (1996), Ramírez et al. (2000), and Fulbright et al. (2006), using spectroscopic observations, and by Zoccali et al. (2003) with a purely photometric method. Among them, the McWilliam & Rich (1994) and Fulbright et al. (2006) analyses deserve special mention because they were the only ones to obtain high-resolution spectra, although only for a small sample of stars (11 and 27, respectively), used to calibrate some previous, low-resolution analysis of a larger sample. The choice of this method was dictated by high resolution spectroscopic surveys being carried out with long-slit spectrographs, thus observing just one or two stars at a time. With the advent of the FLAMES multiobject spectroscopic facility at the VLT (Pasquini et al. 2003) it then became possible to observe a large number of objects simultaneously, at high spectral resolution, a quantum jump in this kind of studies.

⋆ Observations collected at the European Southern Observatory, Paranal, Chile (ESO programmes 71.B-0617 and 73.B-0074).
⋆⋆ Full Table 3 is only available in electronic form at http://www.aanda.org

Table 1. Characteristics of the four bulge fields.

Nr.	Identification	l	b	R_{GC} (pc)	$E(B-V)$	N_{stars}
1	Baade's Window	1.14	−4.18	604	0.55	204
2	$b = -6°$ Field	0.21	−6.02	850	0.48	213
3	$b = -12°$ Field	0.00	−12.0	1663	0.20	104
4	NGC 6553 Field	5.25	−3.02	844	0.70	201

Table 2. Magnitude, color and S/N range of the spectroscopic targets.

Nr.	Identification	$(V-I)$ range	I range	typical S/N @6200 Å
1	Baade's Window	1.53–2.62	14.20–14.70	40–60
2	$b = -6°$ Field	1.41–2.43	14.00–14.50	60–90
3	$b = -12°$ Field	1.10–1.70	13.70–14.93	40–80
4	NGC 6553 Field	2.00–3.00	14.00–14.50	30–60

FLAMES feeds 8 fibers to the UVES high resolution spectrograph, and over 130 fibres to the GIRAFFE medium-high resolution spectrograph. The results of bulge stars observations of 50 K giants obtained with UVES with $R \simeq 45\,000$ have been reported by Zoccali et al. (2006) concerning the oxygen abundance and the [O/Fe] vs. [Fe/H] correlation, and by Lecureur et al. (2007) concerning the abundance of O, Na, Mg, and Al.

This paper is the first of a series devoted to the detailed chemical analysis of a sample of 720 bulge giant stars, in four different fields, observed with FLAMES-GIRAFFE with a resolution $R \sim 20\,000$. Another 220 bulge red clump stars were observed, in the same condition, as part of the GIRAFFE GTO programme (Lecureur et al. 2008). The latter sample is occasionally combined with the present one, in order to investigate some of the systematics and increase the statistics. Taking advantage of the FLAMES link to the UVES spectrograph, 58 target stars were *also* observed at higher spectral resolution ($R = 45\,000$), making it possible to compare abundances derived from medium and high resolution spectra.

2. Observations

Spectra for a sample of K giants in four bulge fields have been collected at the VLT-UT2 with the FLAMES-GIRAFFE spectrograph, at resolution $R \sim 20\,000$. A total wavelength range of ∼760 Å has been covered through the setup combinations HR 13+HR 14+HR 15 (programme 071.B-0617) for fields 1 and 2 in Table 1, and HR 11+HR 13+HR 15 (programme 073.B-0074) for fields 3 and 4. The characteristics of the observed fields, together with the number of target stars contained in each, are listed in Table 1. The total exposure time varies from about 1 h to almost 5 h, depending on the setup and on the star luminosity (targets have been divided into a bright and a faint group) in order to insure that the final S/N of each coadded spectrum is ∼60. In fact, the actual S/N is not identical among the targets of a given field (see Table 2) due to the differences both in magnitude and in the average accuracy of fibre positioning.

2.1. Photometric data

In the color magnitude diagram, these stars are located on the red giant branch (RGB), roughly 1 mag above the red clump (see Table 2), as shown in the lower panels of Fig. 1. The astrometry and the photometric V, I data come from the OGLE catalogue (Udalski et al. 2002) for our Field-1, from archive WFI images obtained within the ESO Pre-FLAMES survey (e.g., Momany et al. 2001) from which our group obtained the stellar catalogue (Field-2 and -3), and from archive WFI images from proposal 69.D-0582A kindly reduced by Yazan Momany, for Field-4. Cross-identification with the 2MASS point source catalogue (Carpenter et al. 2001) allowed us to obtain V, I, J, H, K magnitudes for each of the target stars. Some of the fields contain a globular cluster, namely NGC 6528 and NGC 6522 in Baade's Window, NGC 6558 in the $b = -6°$ field, and NGC 6553 in the eponymous field. Member stars of these clusters will be discussed only marginally here, because they are the subject of dedicated papers (see Barbuy et al. 2007, for NGC 6558).

In order to avoid strong biases in the resulting iron distribution function (IDF) we included targets spanning the whole color range of the RGB at that magnitude. However, the need to maximize the number of targets while avoiding forbidden fibre crossings, makes it impossible to actually fine tune a uniform sampling of the RGB color span. The upper panels of Fig. 1 show as a thick histogram the ratio of the number of targets (dotted histogram) at each color bin, to the available stars (solid histogram). The scale of the thick histogram is shown on the right side of the figure. Since we expect a correlation between the RGB color and the metallicity of the stars, the ideal, unbiased sample would be one with a flat ratio between observed and available stars at each color[1]. As stated above, it is virtually impossible to keep this constraint all the way through the fibre allocation process. For this reason, further below in our analysis we will correct the *raw* IDF for this bias. We will do that in two independent ways, namely: *i)* we randomly remove from the IDF stars belonging to the most populated color bins, until we reach a flat target/available-star ratio; or *ii)* in the less populated color bins we duplicate some randomly-extracted stars, until we reach a flat target/available-star ratio. In both cases we will repeat the process 200 times, in order to minimize stochastic fluctuations in the final star list due to the random extractions, and we combine the results just by merging the 200 star lists. The resulting IDF from the two methods described above are indistinguishable, proving that the method is indeed robust (see Fig. 7 below).

The $V - I$ color was used to obtain photometric temperatures, according to the latest empirical calibration (Ramírez & Meléndez 2005) based on the InfraRed Flux Method. As an additional indicator of the star temperature we measured the strength of the TiO band using an index defined between 6190–6250 Å (band) and 6120–6155 Å (continuum region). The strength of this index indeed correlates very well with the photometric temperatures, for $T_{phot} < 4500$ K, where the TiO band is strong enough to be measured. The TiO index was used in two ways. First, it allowed us to establish that the $V - I$ color was the best one to derive photometric temperatures, as the one showing the smallest dispersion in the correlation between T_{V-I} and T_{TiO}. Second, since we expect that the $V - I$ color is more sensitive to differential reddening variations than the TiO index, for stars cooler than 4500 K, we used the latter to estimate a $(V-I)_0$ color, to be converted into a photometric temperature. The calibration we used to convert the TiO index into a $(V - I)_0$ color was estimated as a linear fit to the observed correlation between the strength of the index and the $(V - I)_0$ obtained assuming a constant reddening for each field (see Table 1). Therefore, the use of the T_{TiO} for the coolest stars only minimizes the effect of the *differential* reddening. Any problem related to the adopted

[1] Note that a region within 2 arcmin from the cluster center was removed both from the available-star and from the target sample.

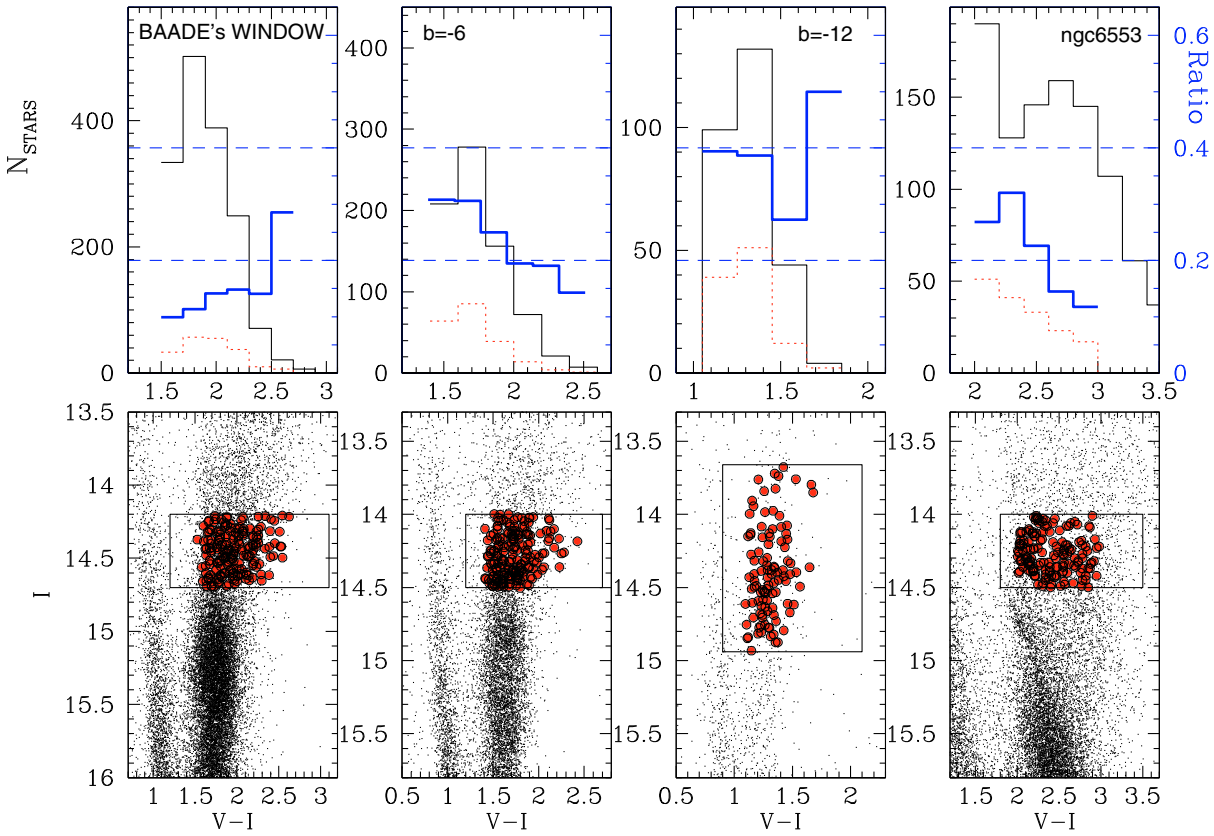

Fig. 1. *Lower panels*: the color magnitude diagram of the four observed fields, with the spectroscopic target stars marked as large filled circles. *From left to right* the fields are: Baade's Window, the $b = -6°$ field, the $b = -12°$ field and the NGC 6553 field. The large box shows the magnitude limits used for target selection, and the color limits of *the upper panels*. *Upper panels*: color histogram of the available stars in the selected target box (thin solid), of the actually observed targets (dotted) and of the ratio of observed to available stars (thick solid). The vertical scale of the latter histogram is shown on the right hand side of *the upper panels*, and two dashed lines have been drawn at 0.2 and 0.4 to help the eye in reading the figure.

color-temperature calibration by Ramírez & Meléndez (2005) will obviously be present also in our TiO-$(V-I)_O$-temperature calibration. Finally, it is worth emphasizing that the photometric temperature has only been used as an initial first guess. The final adopted temperature is the spectroscopic one, derived imposing excitation equilibrium on a sample of ∼60 FeI lines.

Photometric gravity was instead calculated from the classical relation:

$$\log g_* = \log g_\odot + 4 \log \frac{T_*}{T_\odot} + 0.4\,(M_{\rm bol} - M_{\rm bol,\odot}) + \log \frac{M_*}{M_\odot}$$

adopting a mean distance of 8 kpc for the bulge, $T_\odot = 5770$ K, $\log g_\odot = 4.44$, $M_{\rm bol\odot} = 4.75$ and $M_* = 0.85\ M_\odot$. Note that, at each step of the iterative process to converge on the stellar parameters and metallicity, described below, the photometric gravity was re-calculated using the appropriate (now spectroscopic) temperature and metallicity (to compute the V-band bolometric correction, from Alonso et al. 1999) for the star under analysis.

2.2. Spectroscopic data

Individual spectra were reduced with the GIRBLDRS pipeline[2] provided by the FLAMES consortium (Geneva Observatory; Blecha et al. 2003), including bias, flatfield, extraction and wavelength calibration. All the spectra for each star (a number between 1 and 5, depending on the field) were then registered in wavelength to correct for heliocentric radial velocity and coadded to a single spectrum per setup, per star. In each plate, about 20 GIRAFFE fibres were allocated to empty sky regions. These sky spectra were visually inspected to reject the few that might have evident stellar flux, and then coadded to a single sky spectrum. The latter was then subtracted from the spectrum of each target star. The equivalent widths (EWs) for selected iron lines were measured using the automatic code DAOSPEC (Stetson & Pancino, in preparation[3]).

3. Line list

The selection of a clean line list, and the compilation of their atomic parameters, has been done with special care. An initial line list was compiled from NIST (Fuhr & Wiese 2006). Each line was then checked against blends, in the relevant metallicity and temperature range, using synthetic spectra generated with and without the line, using the codes by Alvarez & Plez (1998) and Barbuy et al. (2003). The oscillator strengths log gf of each of the clean lines were then modified by requiring that it would give [Fe/H] = +0.30 on the spectrum of μ Leonis, observed at the Canada-France-Hawaii Telescope with the ESPaDOnS spectrograph, at resolution $R = 80\,000$ and $S/N \sim 500$. The following parameters were determined for μ Leo: $T_{\rm eff} = 4550$ K, $\log g = 2.3$, microturbulence velocity $V_{\rm t} = 1.3$ km s^{-1}. The final line list is thus the same used in Lecureur et al. (2007) with the

[2] Available at SouceForge, http://girbldrs.sourceforge.net

[3] http://cadcwww.hia.nrc.ca/stetson/daospec/

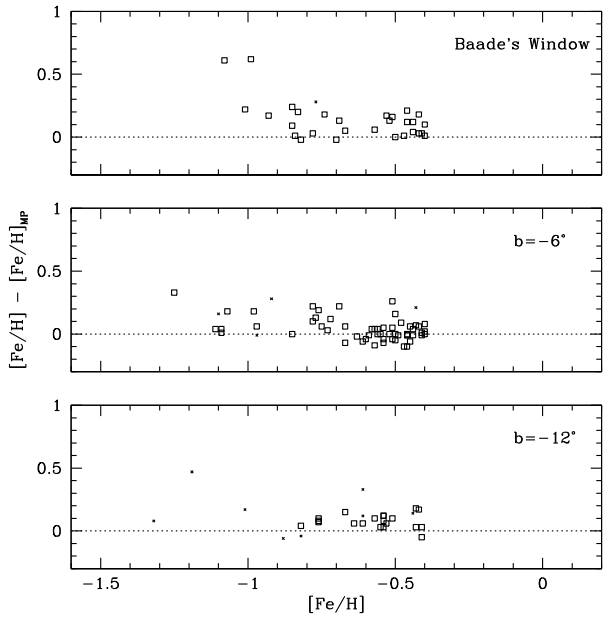

Fig. 2. Comparison between the iron abundance obtained using either the *metalpoor* or the *metalrich* line list, for stars with [Fe/H] < −0.4. Small symbols are stars for which the metal-rich line list was giving very poor results (e.g., it was not possible to converge on excitation equilibrium, or the dispersion of measurements from individual lines was too high) and those stars were thus marked as "low quality".

addition of some more lines in the region covered by the HR 11 GIRAFFE setup (5597−5728 Å) not included in that paper. With the same set of atomic lines we obtained [Fe/H] = −0.52 for Arcturus ($T_{\rm eff}$ = 4300 K, $\log g$ = 2.5 and $V_{\rm t}$ = 1.5 km s^{-1}), and [Fe/H] = −0.02 for the Sun ($T_{\rm eff}$ = 5777 K, $\log g$ = 4.4 and $V_{\rm t}$ = 1.0 km s^{-1}). The damping constants, taken from Coelho et al. (2005) were computed where possible, and in particular for most of the FeI lines, using the collisional broadening theory (Barklem et al. 1998, 2000).

This line list proved effective down to [Fe/H] ∼ −0.8, including lines with a wide range of EWs for all the stars. For more metal-poor stars, however, we started lacking strong lines. A different line list was then compiled, including lines that would be too strong in μ Leo, but of intermediate strength in relatively metal poor stars. This one was produced with the same criterion described below, except that we have kept the NIST $\log gf$s. In order to ensure a smooth transition between the so called *metalrich* and the *metalpoor* line list, we measured the metallicity of Arcturus, from a UVES spectrum (Bagnulo et al. 2003) with both, and switch from one to the other at [Fe/H] = −0.4, where we check that the two would give consistent results. The metallicity of Arcturus with the *metalpoor* line list, and the same parameters listed above, is [Fe/H] = −0.55.

Figure 2 shows the difference between the [Fe/H] values resulting from the use of the *metalrich* or the *metalpoor* line list, for stars with [Fe/H] < −0.4. It can be seen that at the transition region (−0.6 < [Fe/H] < −0.4) the systematic difference is 0.09 dex, 0.01 dex and 0.08 dex, for Baade's Window, the b = −6° field and the b = −12° field, respectively. For more metal poor stars the difference obviously increases, because the *metalrich* line list is clearly not appropriate for them.

Finally, in order to complete the analysis of possible systematics due to the adopted line list, we measured the metallicity of Arcturus by selecting only the wavelength ranges of the two setup combinations we used for our targets, namely HR 13+HR 14+HR 15 or HR 11+HR 13+HR 15. The difference in [Fe/H] is +0.01 dex, the first setup combination giving higher metallicity, both with the *metalpoor* and with the *metalrich* line list. The value quoted above for the metallicity of Arcturus ([Fe/H] = −0.52) refers to the HR 13+HR 14+HR 15 setup combination.

4. Abundance analysis

LTE abundance analysis was performed using well tested procedures (Spite 1967) and the new MARCS spherical models (Gustafsson et al. 2003; available at http://www.marcs.astro.uu.se/). Excitation equilibrium was imposed on FeI lines in order to refine the photometric $T_{\rm eff}$, while photometric gravity was imposed even if ionization equilibrium was not fulfilled (cf. Zoccali et al. 2006). The microturbulence velocity ($V_{\rm t}$) was found by imposing a constant [Fe/H] for lines of different expected strengths (predicted EWs for a given stellar model). The reason for the latter choice is that, when plotting derived metallicities versus observed EWs, the obvious correlation of the errors (a too high EW would give a too high [Fe/H], and vice versa) would lead us to detect a positive slope, hence to increase the $V_{\rm t}$ (Magain 1984). The effect may be negligible with very high S/N, high resolution spectra (i.e., when the errors on the EWs are also negligible) but we verified that it would introduce a significant systematic error in the measurements of the present GIRAFFE spectra. Extensive discussion of this effect can be found in Lecureur et al. (2008).

Finally, once converged on the best stellar parameters, we calculate the [Fe/H] of each star as a weighted mean of the line-by-line measurements. The weight associated to each line is given by the inverse square of its abundance error, as derived from the error in the measured EWs.

5. Estimates of metallicity uncertainties

In this section we discuss all the available information about the error associated to the [Fe/H] of each star. Some of our tests will quantify only the statistical errors, some others will quantify a combination of part of the systematics and the statistical errors. Finally, we will try to combine all this information together in order to estimate how far we can go in the interpretation of apparent features of the obtained IDFs.

5.1. Line-to-line dispersion

Figure 3 shows the scatter in the line-by-line [Fe/H] measurement, divided by the square root of the number of lines, versus [Fe/H]. This is a fairly reasonable estimate of the statistical (line-to-line only) fluctuation associated with each [Fe/H] value. Clearly, the more metal rich the star, the more crowded is the spectrum, hence the higher the dispersion of [Fe/H] from individual lines. Baade's Window's stars show the largest scatter, likely due to the lower S/N of those spectra, caused by the lower accuracy of the astrometry (from the OGLE catalogue) used to position the fibres. In any case, the statistical error from the dispersion of individual lines is less than 0.06 dex for Baade's Window, and less than 0.04 dex for the other fields.

5.2. Degeneracy in the stellar parameters

Because of a mistake in the fibre allocation, in the b = −12° field a sample of ∼100 stars was observed twice, instead of switching

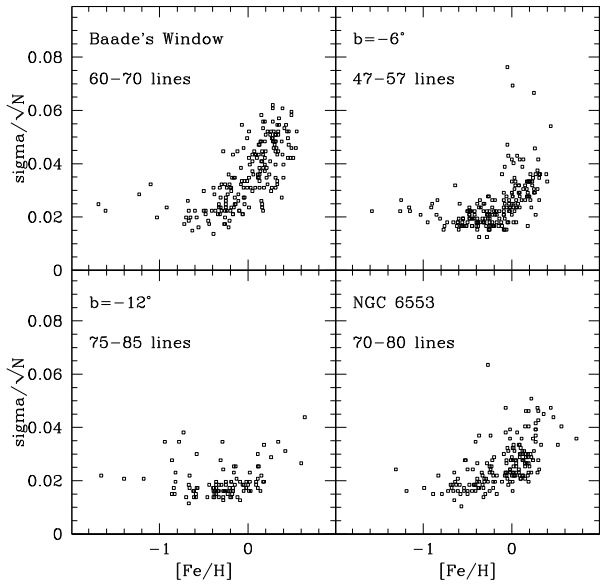

Fig. 3. The error on the mean [Fe/H] of each star, due to the line-to-line dispersion. The minimum and maximum number of FeI lines found in each star is indicated in the figure labels.

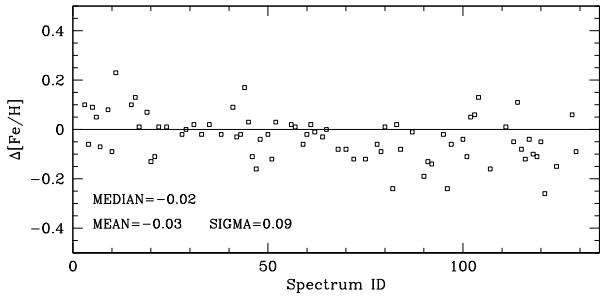

Fig. 4. The difference in [Fe/H] between the two independent measurements of the two repeated sets of spectra in the $b = -12°$ field.

to the next target sample. This unintentional duplication, on the other hand, turned out to be very useful to estimate the *repeatability* of our measurements. The two sets of spectra for the same stars have been reduced in a fully independent way, as if they were different stars, and the stellar parameters were also derived independently. Thus, the differences in the metallicity obtained for the same star is not only due to statistical fluctuations, but also to possible differences in the adopted parameters. Figure 4 shows the difference in the [Fe/H] of each star, from the two sets of observations. The figure label shows the mean, median, and spread of the distribution. We checked for correlations of the Δ[Fe/H] against any stellar parameter ($T_{\rm eff}$, $V_{\rm t}$, [Fe/H], S/N, ...) but to our great surprise, the only quantity that showed a mild correlation with the [Fe/H] difference is the spectrum ID, meaning the fibre position along the slit. Specifically, more than a *trend* what we see is a systematic offset between the first ∼65 stars ($\langle\Delta$[Fe/H]$\rangle \approx 0$) and the next ones ($\langle\Delta$[Fe/H]$\rangle \approx -0.07$). No physical property of the star is associated with this parameter, and it is unlikely that any instrumental effect could explain this behaviour. The difference is instead due to the *fluctuations* in the subjective process of converging to the best stellar parameters. In other words, since the stellar parameters, and in particular the temperature and the microturbulence velocity, produce similar results on the line-by-line [Fe/H] abundances, it is possible to converge on two different model atmospheres

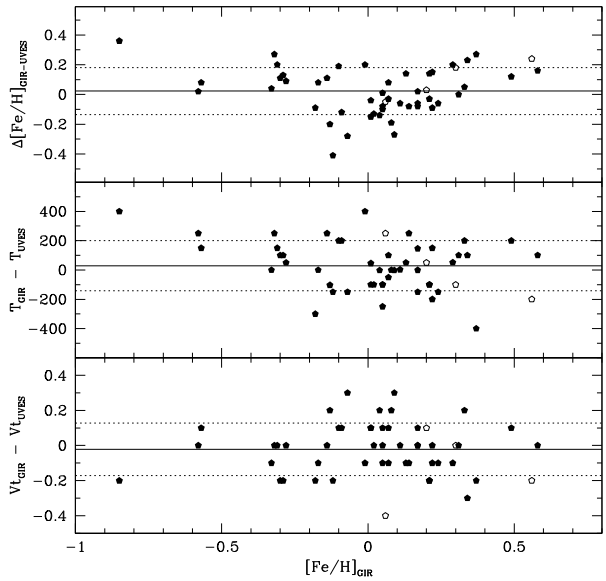

Fig. 5. Comparison between the measured iron abundances, temperature and microturbulence velocity in the stars observed both with UVES and GIRAFFE. Open symbols are stars with larger dispersion in the line-by-line iron measurements (mostly metal rich stars). The mean systematic difference (solid line) and the $\pm1\sigma$ spread around it (dotted lines) are shown.

(i.e., with both different $T_{\rm eff}$ and different $V_{\rm t}$, compensating each other) while preserving both the excitation equilibrium and a constant abundance with EWs. The two models will give slightly different mean iron abundance. Therefore, the resulting [Fe/H] may differ by as much as ≈0.07 dex, depending on whether one starts by iterating on $T_{\rm eff}$ until reaching excitation equilibrium, then fixing the required $V_{\rm t}$, or one proceeds in the opposite direction, first fixing $V_{\rm t}$, and then iterating on $T_{\rm eff}$. According to our records, this change of procedure occurred in fact around spectrum Nr. 65. While we could have re-analyzed the stars keeping a uniform procedure, we preferred to leave track of the effect that such difference in the analysis has caused on the resulting [Fe/H]. Hence, Δ[Fe/H] < 0.07 dex, is a good estimate of the mean fluctuations due to the subjective part of the analysis.

On the other hand, for stars with metallicity close to solar, a systematic error of ±200 K in the adopted $T_{\rm eff}$ (and corresponding change in the gravity calculated from Eq. (1)) implies a Δ[Fe/H] $= ^{+0.18}_{-0.15}$ dex, for a star with $T = 4800$ K, and Δ[Fe/H] $= ^{+0.07}_{-0.03}$ dex, for a star with $T = 4300$ K. A systematic error of ±0.2 in the microturbulence velocity implies a Δ[Fe/H] $= ^{-0.12}_{+0.13}$ dex, for both cool and warm stars. A more extensive discussion of systematic errors in this kind of analysis is presented in Lecureur et al. (2008).

5.3. Stars observed with UVES

Figure 5 shows, for the stars observed also at high resolution with UVES, the comparison between resulting iron abundances (upper panel) and the most relevant parameters (middle and lower panels). We note that the stars observed with UVES were 58 in total (cf. Table 1 in Lecureur et al. 2007): 13 were Baade's Window clump, and another 13 were giants, 11 more giants were observed in the $b = -6°$ field, 7 in the $b = -12°$ field and 14 in the NGC 6553 field. However only 50 of them were discussed in Zoccali et al. (2006) and 53 in Lecureur et al. (2007) because

those studied focused on the analysis of a few specific lines, sometimes heavily blended with telluric lines.

From the 58 UVES stars, here we exclude from Fig. 5 the 7 stars in the $b = -12°$ field because they were never re-observed with GIRAFFE, and one more clump star that also failed to be reobserved with GIRAFFE. We are thus left with 50 data points. Among them, open symbols are stars with large dispersion in the line-by-line iron determination, mostly high metallicity stars, and most likely due to line crowding.

The systematic offset is negligible in all the panels. The scatter, again representative of the statistical error, is σ[Fe/H] = ±0.16, consistent with our estimates above. The largest scatter is in the adopted excitation temperature, revealing that this parameter is constrained to no better than ±200 K.

5.4. Globular cluster stars

Yet another independent test on the internal precision of our analysis is offered by the stars which are members of the globular clusters in these fields. The left panels of Fig. 6 show a plot of radial velocity versus metallicity for all the stars in our fields (in a narrow range of radial velocity and metallicity) together with globular cluster stars, shown here as filled triangles. The location of cluster stars in the field of view of FLAMES is shown on the right side of the plot. Cluster members were selected as target stars having [Fe/H] within ±0.2 dex from the cluster mean, radial velocity within ±10 km s^{-1} from the mean, and located within 2 arcmin from the cluster center. Baade's Window contains 7 stars belonging to the metal-poor cluster NGC 6522, and only one member of NGC 6528, at solar metallicity and radial velocity close to 200 km s^{-1} (not shown here). The field at $b = -6°$ contains six members of NGC 6558 (Barbuy et al. 2007). Finally the NGC 6553 field contains the eponymous cluster, but its position in this plot falls near the center of the distribution of the field stars, thus it is harder to discriminate cluster from field, and for this reason the metallicity spread of NGC 6553 *putative* members is not considered here. Cluster stars should have identical velocity and composition, thus the observed spread in this plot is a measure of our (mostly statistical) error. For NGC 6522 and NGC 6558 the 1σ spread for cluster stars is σ[Fe/H] = 0.12 and σ[Fe/H] = 0.15, respectively.

A complete analysis of the chemical abundances of cluster stars has been presented in Barbuy et al. (2007) for NGC 6558, and it is in preparation for NGC 6522. What we show here is the iron content of cluster stars, as measured considering them just like all the other field stars (e.g., adopted distance and reddening are the same as the mean ones for the bulge) and the details of the analysis, such as sigma clipping in Fe lines, etc., are suitable to be extended to all the target stars. For this reason, the actual metallicity of cluster stars derived here is not as accurate as it is in the dedicated papers, though well within our 1 sigma error bar. Cluster stars are shown here with the only purpose of helping estimating our error on individual [Fe/H] measurements.

In summary, the three independent estimates of the internal error via *i)* repeated and independent analysis; *ii)* comparison with the UVES results; and *iii)* globular cluster stars, indicate σ[Fe/H] = 0.09, 0.16, and 0.12 dex, respectively. All those estimates include the smaller (<0.06 dex) statistical error due to line-to-line dispersion, but each of them includes only a subset of all the possible causes of errors. Putting together the different tests, and considering that some of the systematics (e.g., possible non LTE effects, errors in the model atmospheres themselves, etc.) have not been taken into account here, we can conclude that ±0.2 dex is a conservative estimation of our uncertainty on the metallicity of the individual star, including both the effect of statistics and systematics.

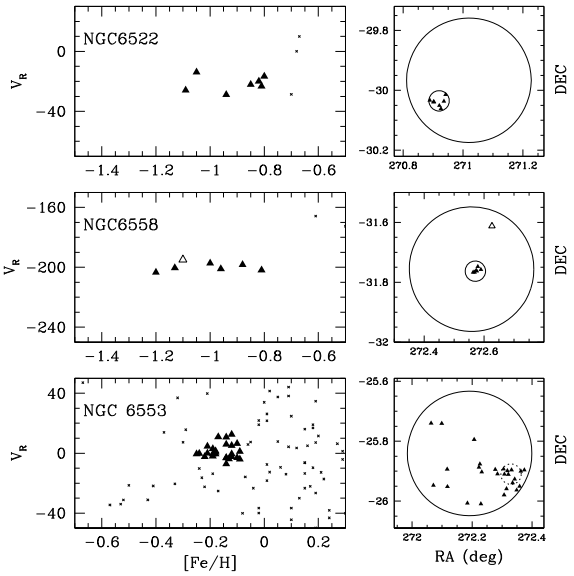

Fig. 6. *Left panels*: iron abundance versus radial velocity for globular cluster stars included among our targets (filled triangles). Bulge field stars are also shown as small symbols, in order to emphasize that while NGC 6522 and NGC 6558 can be easily separated from field stars, some ambiguity is present in the selection of stars belonging to NGC 6553, due to its near solar metallicity and low radial velocity. *Right panels*: position of cluster stars with respect to the FLAMES field of view (large circle). The small circle has a radius of 2 arcmin around the cluster center. One star, shown as an open triangle in *the middle panel*, has metallicity and radial velocity similar to the other NGC 6558 members, but it is very far away from the cluster center, making it unlikely to be a member. *The lower right panel* shows once again that unambiguous identification of cluster members in NGC 6553 is very hard.

6. The distribution functions of the iron abundance

The IDFs obtained in the three fields along the bulge minor axis are shown in Fig. 7, and the corresponding data are given in Table 3. The thick histograms show the raw IDFs, while the shaded and the thin open one are the IDF corrected from the color bias discussed in Sect. 2.1, using method *i)* and *ii)*, respectively. The differences are in fact very small, fully consistent with our error bars, but we judged important to prove to ourselves that this kind of bias was negligible, given the way our targets were selected. We do not show here the IDF for the field around NGC 6553 due to the fact that, as shown in Fig. 1, this field has the strongest differential reddening, and none of the reddest stars were included in our target list. Thus, we believe that, if there is any bias, in NGC 6553 our sample may be biased against the most metal-rich stars. In addition, in order to evaluate the fraction of stars sampled at each color, we had to exclude cluster stars both in the total color magnitude diagram and in the target sample. This task proved extremely hard in the NGC 6553 field, due to the dimension and centrality of the cluster. Finally, as shown in Figs. 6 and 15, both the metallicity and the radial velocity of cluster stars sit just in the middle of the distributions of field stars. For these reasons, we will not include the IDF of this field in our discussion of the general bulge iron content. On the other hand, the NGC 6553 field, thanks to its largest extinction, will prove useful in our analysis of the disk contamination (see discussion in Sect. 8).

Table 3. Stellar parameters and iron abundance of all the program stars.

QF[a]	ID	OGLE-ID	RA	Dec	V	$V-I$	$\log g$	V_t	$T_{\rm eff}$	[Fe/H]	σ^b	Cluster?
Baade's window												
0	2	423342	18:03:50.00	–29:55:45.20	16.36	1.805	1.99	1.3	4650	0.46	0.38	–
0	3	423323	18:03:48.39	–29:56:27.10	16.10	1.846	1.59	1.5	4200	–0.48	0.18	–
0	4	412779	18:03:43.18	–29:59:40.10	15.91	1.667	1.93	1.5	4850	–0.37	0.18	–
2	5	412803	18:03:46.14	–29:58:30.00	16.40	2.083	1.52	1.3	4000	0.51	0.34	–
0	6	423359	18:03:47.03	–29:54:49.20	16.17	1.768	1.92	1.4	4650	–1.23	0.23	–
...	...	...	...	...	...	...	...	...	...	...	...	...

[a] QF is a subjective quality factor, classifying stars into good (0), bad (2) and intermediate (1), according to how unique/degenerate the convergence into the final model atmosphere proceeded.
[b] Line-to-line dispersion around the mean [Fe/H].

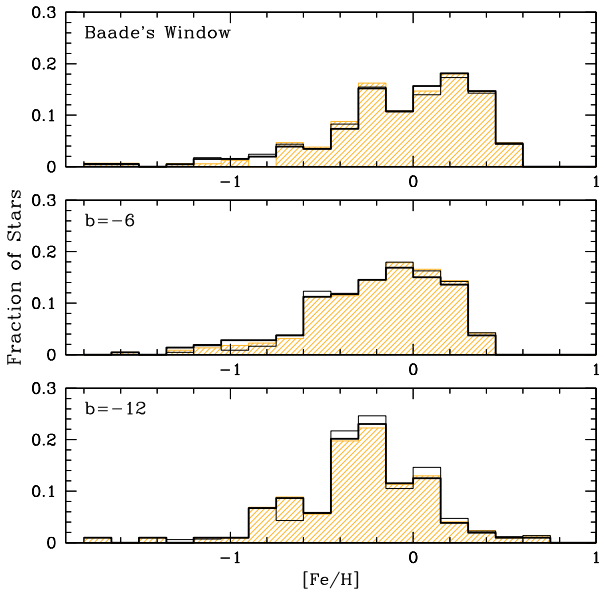

Fig. 7. The raw IDF (thick histogram) compared with the IDF corrected for color bias, according to method *i)* (shaded histogram) and method *ii)* (thin histogram) discussed in Sect. 2.1.

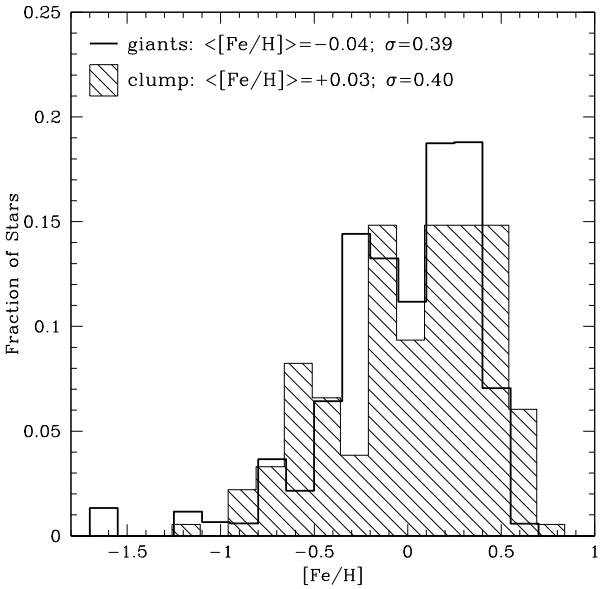

Fig. 8. Comparison between the IDF of Baade's Window as derived from giant and red clump stars, the latter from Lecureur et al. (2008).

As mentioned before, for the Baade's Window field two independent (but homogeneous) sets of data are available: the 204 giants discussed here, and another ∼200 red clump giants observed within the guaranteed time reserved to the FLAMES French consortium. The latter, extensively discussed in a companion paper (Lecureur et al. 2008), have been reduced in a very similar way as the present data, and Fig. 8 shows the comparison between the IDFs of the two samples. Although some differences seem to be present between the two distributions[4] Note that the smaller amount of metal poor stars in the clump IDF is expected, since metal poor stars would not be found in the red clump but on the blue side of the horizontal branch (HB). However, there are really few metal-poor stars even in the giant IDF (only 6 out of 204 stars have [Fe/H] < -1.0) hence we consider this bias rather negligible. Therefore, in the following discussion the two sets will be combined and the quoted Baade's Window IDF will result from the independent analysis of a total of ∼400 stars.

[4] As discussed in Lecureur et al. (2008), the analysis of the clump stars has been done with an automatic procedure, based on the same prescriptions followed here in a manual way. A discrepancy as large as that shown in Fig. 4, can be expected between the two IDFs, for the same reason, and it is still small when compared to the total uncertainty presented above: in fact, the means of the two distributions agree within 0.06 dex.

Figure 9 shows the comparison with some of the previous determinations of the IDF of bulge fields. The left panel compares the present IDF (shaded) with the photometric one by Zoccali et al. (2003), both relative to the field at $b = -6°$. The two IDFs are different, especially at high metallicity, possibly due to the lack of calibrating template red giant branches for solar metallicity and above. At the opposite end of the IDF, the less prominent metal poor tail with respect to Zoccali et al. (2003) can be ascribed to an innate limit of the photometric method, as the RGB color becomes less and less sensitive to [Fe/H] at decreasing metallicity, hence even small color errors imply large errors in the derived [Fe/H]. The right panel shows the comparison with the spectroscopic IDF for Baade's Window from Fulbright et al. (2006), as obtained from the recalibration of the Sadler et al. (1996) IDF. It can be seen that in both cases the present spectroscopic IDF is appreciably narrower than previous results. In a sense, this is consistent with our effort at reducing the errors on individual measurements. However, Fig. 9 also shows as a solid histogram the 27 stars that were actually measured by Fulbright et al. (2006) at high spectroscopic resolution. Those are the stars that were used to recalibrate the Sadler et al. (1996) IDF obtained from low resolution spectra. It can be appreciated that none of the 27 stars has [Fe/H] > 0.5, despite their selection of 3 stars with [Fe/H] ≥ 0.5 in Sadler et al. (1996). The discrepancy at the metal rich end is in a region where the Fulbright et al. calibration

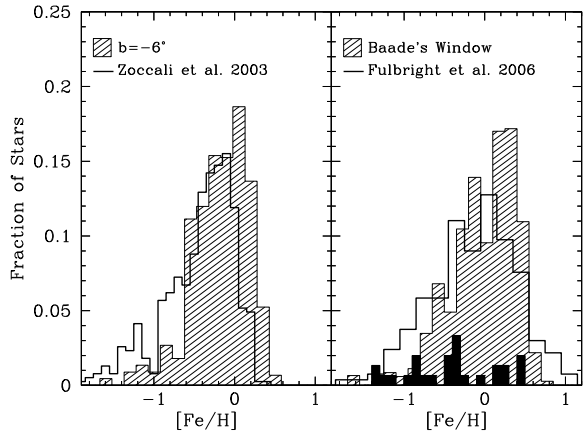

Fig. 9. The derived IDF is compared with previous measurements, in the corresponding fields. *Left*: the photometric IDF by Zoccali et al. (2003) obtained in the $b = -6°$ field observed here. *Right*: the spectroscopic IDF by Fulbright et al. (2006) in Baade's Window is compared with the present results. Also shown as a black solid histogram (arbitrarily normalized) is the IDF of the 27 stars actually observed by Fulbright et al. (2006) at high spectral resolution.

was in fact used in extrapolation. In addition, the strong Mg_2 features found in the most metal-rich and cooler stars are contaminated by TiO lines (see, e.g., Fig. 13 by Coelho et al. 2005) and the high end of the Sadler et al. (1996) IDF itself probably has an overestimated high metallicity tail.

Less obvious is the interpretation of the discrepancy at low [Fe/H] with respect to the IDF by Fulbright et al. (2006). The high resolution sample of Fulbright et al. (2006) contains four stars with [Fe/H] < -1, so that we know that the total sample (88 giants from Rich 1988) from which those stars were picked (with an on-purpose flat IDF) had to contain at least that number of stars. This would mean that we would expect some ∼9 stars in our RGB sample, whereas we observe only 6. Although different, the two numbers are still compatible within the very low statistics considered here.

On the other hand, with some simple calculations we can check that the number of metal poor stars in the IDF is consistent with the number we expect from independent sources. First, it is well known that the bulge contains RR Lyrae stars, classical tracers of the metal poor population. From the MACHO (Alcock et al. 1998) and OGLE II (Collinge et al. 2006) surveys, we know that there are ∼30 RR Lyrae per FLAMES field, at $b = -6°$. The total number of red clump stars in this field can be estimated from the CMD in Fig. 1: there are 4090 stars within a box with $1.3 < (V - I) < 2.1$ and $14.5 < I < 15.5$. This box includes both the red clump and the RGB at that level. From the synthetic CMD presented in Zoccali et al. (2003, their Fig. 20) we know that only 67% of them, i.e., 2740 stars, are actually red clump stars. Therefore, in a FLAMES field there are 30 RR Lyrae stars for every 2740 red clump stars, i.e., 1% of the total number of stars are expected to have [Fe/H] < -1. There could still be more metal poor stars that end up too blue in the horizontal branch to pulsate as RR Lyrae. Their number can be estimated from Busso et al. (2005), who obtained spectra of candidate extreme blue HB stars in the bulge. Out of their 28 targets, 15 (57%) turned out to be true blue HB stars. There are 51 extreme blue HB candidates in the CMD of the complete FLAMES field, hence $51 \times 0.57 = 29$ of them were confirmed spectroscopically. This number is almost identical to the number of RR Lyrae, hence another 1% of the total number of bulge stars are expected to be metal poor enough to end up in the extreme blue HB.

All in all, based on the known fraction of stars in the extreme blue HB and in the RR Lyrae gap, we expect that at least 2% of the total number of stars in the bulge should be metal poor, say with [Fe/H] < -1. This percentage has to be taken as a lower limit, because while we can easily count RR Lyrae and extreme HB stars, there is a narrow range in color, corresponding to A-type blue HB stars that is heavily contaminated by the disk main sequence.

Our IDF at $b = -6°$ is based on ∼200 stars and 6 of them have [Fe/H] < -1, fully consistent with the 4 (at least) expected from the above calculation. Therefore, even if the number of metal poor stars in the IDF presented here might seem very small, for example compared with previous measurements or with a simple, closed box model (see below), it is consistent with the number of expected metal poor stars in the bulge estimated from independent evidence.

In closing this section it is worth mentioning that Johnson et al. (2007, 2008) and Cohen et al. (2008) have recently measured the chemical abundances of three bulge dwarfs during a microlensing event. They find metallicities close to [Fe/H] ∼ +0.5 for all the stars, a value too high to be consistent with random extraction of three stars from our IDF. This discrepancy is very puzzling, although it is fair to mention that several microlensed bulge dwarfs had been observed by Cavallo et al. (2003) finding metallicities consistent with ours. Speculations have been made that dwarf stars, being unevolved, might give the "true" IDF, as opposed to giants, whose evolution might actually depend on their metallicity. However, at present there is no indication that supports such major differences in the evolutionary path of a star at [Fe/H] = −1.0 with respect to one at [Fe/H] = +0.5. As discussed in Zoccali et al. (2003, their Fig. 13) the metallicity dependence of the evolutionary flux along the RGB (i.e., of the number of stars reaching the RGB per unit time) and of the stellar RGB lifetime has opposite trends, so that stars of all metallicities are equally represented along the RGB. Cohen et al. suggest that higher mass loss in metal rich stars would cause them to leave the RGB before reaching the level of our samples (at $I \sim 14.5$), then evolving to the helium white dwarf stage. Were that true, one would expect a drop in the RGB luminosity function which is not observed (Zoccali et al. 2003, their Fig. 21).

We note that the extremely high amplification of these microlensing events (>300) indicates that a different amplification might have taken place between the limb and the center. The lens model and the model atmosphere should take these effects into account.

6.1. Disk and halo contamination in the bulge fields

In this section we present our estimates for the contamination in the survey fields coming from the thin and thick disk, and from the halo. The working tool for these estimates is an updated version of the Besançon Galaxy model (Robin et al. 2003) kindly computed by M. Schultheis for us. Simulated CMDs have been constructed for the three fields along the bulge minor axis. Small adjustments were made in the assumed reddening law in order to insure that the simulated red clump would coincide in color and magnitude with the observed one. The resulting model CMDs, together with the observed ones, are shown in the upper panels of Figs. 10–12. Clearly, the model CMDs reproduce reasonably well many characteristics of the observed CMDs, but significant differences are also evident. For example, the giant branches are

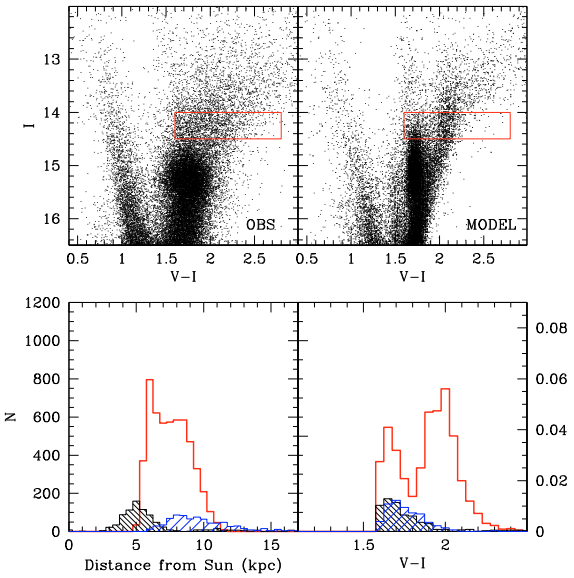

Fig. 10. *The upper panels* show the observed and model CMD for the Baade's Window field, together with the box where the targets were selected. *The bottom panels* show the distance and color distribution of bulge stars (open histogram) and of thick (light dashed) and thin disk (heavy dashed). The disk histograms are scaled to the contamination fraction – with respect to the total number of stars – shown in the y-axis on the right end side of the plots.

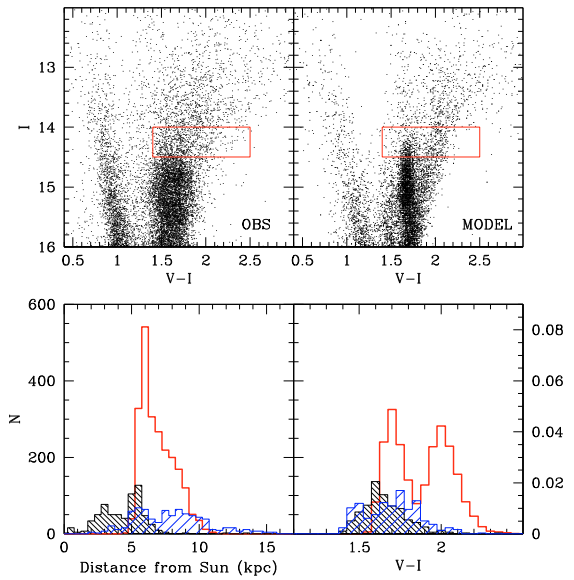

Fig. 11. Same as Fig. 10 for the field at $b = -6°$.

much broader in the data than in the model, possibly because the model does not incorporate small scale differential reddening. Thus, the relative contributions of the various galactic components to the star samples in the various fields need to be taken with caution. However, it is still the best tool available to analyse the expected contamination of our sample from (however poorly) known galactic components on the line of sight.

Stars inside the observed target box were selected in the model CMD, and their distribution in distance, color, and stellar parameters were analysed. The lower panels of Figs. 10–12 show those distributions in distance and color. The raw histogram of bulge stars is shown here, while the disk star histograms are scaled to the fraction of the total number of stars,

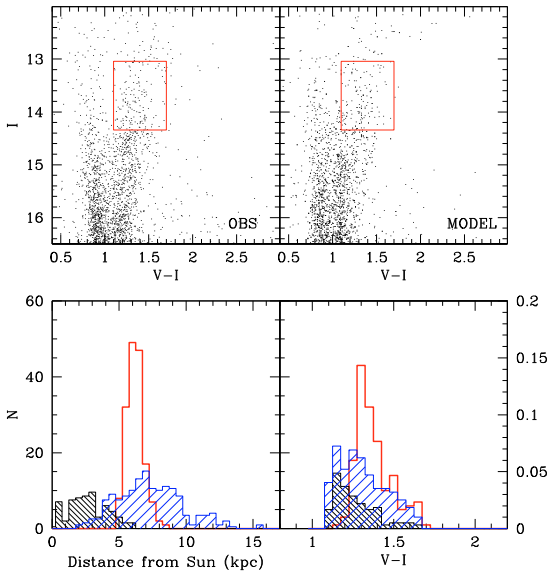

Fig. 12. Same as Fig. 10 for the field at $b = -12°$.

reported in the scale on the right side of the lower right box. We emphasize, then, that disk and bulge here are not shown in the same scale, in order to make the disk histograms more visible. The $V-I$ histogram of bulge stars in the model shows a clear bimodality due to the inclusion of some clump stars – those on the near side of the bulge – and a small number of asymptotic giant branch stars. On the other hand the data do not show a bimodality in the color distribution. The discrepancy may be ascribed to the specific assumptions in the Besancon model, such as the red clump luminosity, color, and the bulge density law.

Particularly interesting is the distance distribution, because it helps understanding the evolutionary phase, thus the gravity, of the contaminating stars. One can see, for instance, that in Baade's Window the Besançon model predicts contaminating thick disk stars to be located at the same distance of the bulge. Therefore, for these stars the photometric gravity we assume in the analysis is correct, hence so is the derived iron abundance. On the other hand, the iron abundance alone cannot help us discriminating possible thick disk stars against the bulge ones. It is also important to remark that, if the model is correct, and the thick disk stars contaminating our sample are those as far away as the bulge (or even on the other side), our present knowledge of the thick disk characteristics (age, metallicity, scale height and density) at that position is very poor. Actually, the predicted thick disk stars within the bulge are the result of the assumption in the Besançon model that the thick disk follows an exponential radial distribution, then peaking at the Galactic center.

Contaminating foreground thin disk stars are estimated to be giant stars (not dwarfs as one might naively expect) located mostly between 2 and 5 kpc from the Sun.

The contamination from the halo population turns out to be between 0% and 2% in all the fields (see Table 4), hence it can be safely neglected.

7. The IDF as a function of color

The combination of the metallicity, kinematic and color information for each target star permits a better understanding of the behaviour of the different components of the inner Galaxy.

The left panels of Fig. 13 show the IDF of the NGC 6553 field in different color bins, from blue (bottom) to red (top) as

Table 4. Disk and halo contamination percentage in each field, relative to the total number of stars in the target box.

Field	Thin disk	Thick disk	Halo
Baade's Window Clump	3.2 ± 0.1	5.8 ± 0.1	0.1 ± 0.02
Baade's Window RGB	6.5 ± 0.3	4.8 ± 0.3	<0.1 ± 0.06
$b = -6°$ Field	9.8 ± 0.5	11.5 ± 0.6	0.4 ± 0.10
$b = -12°$ Field	18.9 ± 1.8	59.0 ± 2.1	1.5 ± 0.50

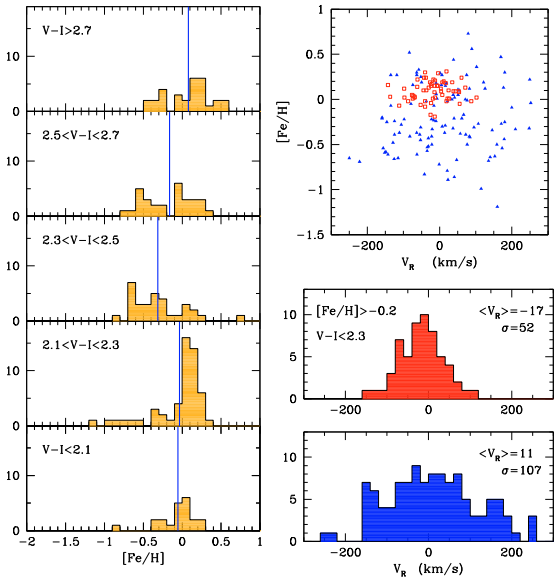

Fig. 13. *Left*: IDF for the NGC 6553 field as a function of color, from the bluest stars at *the bottom* to the reddest stars at *the top*. A vertical line marks the mean of the distribution. *Upper right*: metallicity versus radial velocity for individual stars. Cluster stars have been excluded from all these plots. Empty squares are stars with $V - I < 2.3$, and [Fe/H] > −0.2, while all the other stars are filled triangles. *Middle right*: radial velocity distribution for stars with $V - I < 2.3$ and [Fe/H] > −0.2 (empty squares above). Mean and sigma of the distribution are shown in the figure label. *Bottom right*, same as above for all the other field stars (small filled triangles in *the upper right plot*).

indicated in the labels. It is well known that, were the stars all at the same distance, i.e. belonging to the bulge, then more metal rich giants should be redder. Therefore, the IDF should be progressively shifted to the metal rich side for increasingly redder color bins (upwards in the plots), with some possible spread introduced by differential reddening. This is approximately true, except for the two bluest color bins, that unexpectedly contain only very metal rich stars. If one looks at the radial velocity distribution of those stars (open squares in the upper right plot, and middle histogram) it is clear that they are a colder distribution, with velocity dispersion of 52 km s^{-1}. On the contrary, all the other stars, shown as filled triangles in the upper right plot, have a velocity dispersion of 107 km s^{-1}. Note that suspected clusters stars are not included in any of these plots. Everything suggests that the bluest stars in the CMD are in fact contaminating (thin?) disk stars, located on the blue side of the target box just because they are on average closer to us. In fact, there would be no reason to expect that the most metal rich *bulge* stars should lie preferentially on the blue side of the CMD. Indeed, also the Besançon model predicts disk stars to be always on the blue side of our CMD target box (Figs. 10–12).

In this particular field this effect is more evident than in the other ones because of the larger interstellar extinction all along the line of sight, allowing a color separation between bulge and disk. The important conclusion that can be drawn from this exercise is that the contaminating (thin?) disk has a very metal rich IDF, quite different from that measured in the solar neighborhood. It seems that the contaminating disk is closer than the bulge (bluer in the CMD) but still quite far away from us. The existing disk radial metallicity gradient, then, may explain its higher metallicity with respect to the solar neighborhood.

8. A radial metallicity gradient in the bulge

The final IDFs for the three fields along the bulge minor axis are shown in Fig. 14. Overplotted to the metallicity distribution of bulge stars (histograms) are two gaussians qualitatively showing the estimated contamination by thick and thin disk. The gaussians have indeed the mean and sigma values characteristics of the thick (Reddy et al. 2006) and thin disk (Nordström et al. 2004) IDF, in the solar neighboorhood. As discussed above, very likely the contaminating disk stars are closer to the bulge than to us, but the disk radial gradient for giant stars, i.e., intermediate-age and old disk, has never been measured, hence where exactly these gaussians would lie is not very well known.

Baade's Window. The IDF for this field has been derived from the combination of both clump and giant stars (∼400). Despite the uncertainty on the mean metallicity of the contaminating disk stars, it is clear that their number is negligible in this field.

Field at $b = -6°$. The IDF for this field has been derived from 213 giant stars. Again, the relative disk contamination is low in this field, and would not have a significant impact on the shape of the derived bulge IDF. The comparison with Baade's Window reveals a difference in the mean metallicity, suggestive of a radial metallicity gradient, with the IDF mean value going from $\langle$[Fe/H]$\rangle = +0.03$ at $b = -4°$ to $\langle$[Fe/H]$\rangle = -0.12$ at $b = -6°$. More specifically, it would seem that rather than a solid shift towards more metal poor mean values, it is the metal rich stars that gradually disappear, while the metal poor ones are always roughly in the same position. On the same line, it is interesting to note that there is some indication of a bimodality in the IDF of this field.

Field at $b = -12°$. The interpretation of the IDF for this field, resulting from the observations of 104 stars, is a lot more complicated due to the highest fraction of contaminating disk stars. In this case it is more important to establish what should be the mean metallicity of the contaminating stars. Regarding thick disk stars, the Besançon model predicts them to make up about 60% of the observed stars. However, if thick disk stars are as metal poor as they are seen in the solar neighboorhood, they cannot be as many, just because we do not see as many metal poor stars at all. If the inner thick disk is as metal poor as it is in the solar neighborhood, it cannot account for more than 30% of the total number of stars. This (30%) would be the metal poor gaussian shown in the lower panel. Alternatively, thick disk stars are a bit more metal rich than in the solar neighborhood, probably because they are closer to the center (Fig. 12). Then in this case they could be as many as 60%, perhaps. Regarding thin disk stars, they are expected to make the 20% of the total number of stars. In this case we are more inclined to think that they should lie at the metal rich end of the distribution, because: *i)* it will be shown in Fig. 13 that the contaminating thin disk seems to be indeed very metal rich; and *ii)* because Fig. 15 shows that there

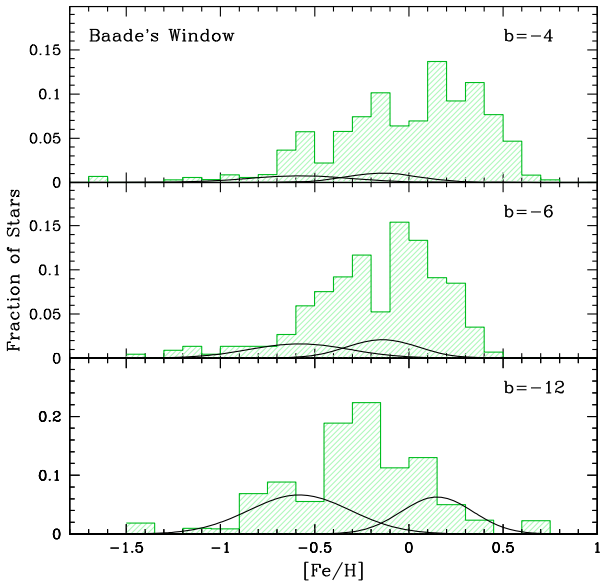

Fig. 14. The obtained IDFs for the three fields along the bulge minor axis, from the innermost one (Baade's Window, *top*) to the outermost one (*bottom*). The gaussians show the IDF of contaminating thick and thin disk stars, normalized to the expected contamination fraction, according to the Besançon Galaxy model. The thick disk contamination percent in the lower panel has been reduced at 30% (as opposed to the 60% predicted by the model) in order to match the number of observed stars with [Fe/H] < −0.5. See text for details.

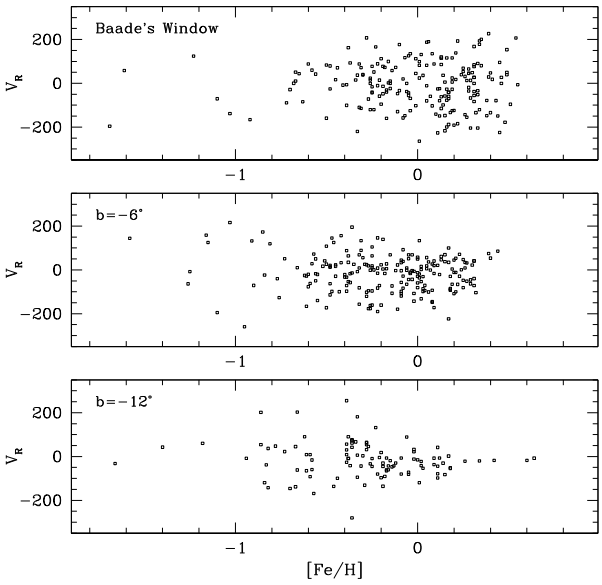

Fig. 15. Metallicity versus radial velocity for individual stars in the three bulge fields along the minor axis. Globular cluster stars shown in Fig. 6 have been removed from this plot.

is a very cold component at the metal rich end of this field. All in all, while it is impossible to conclude what the true bulge IDF is in this field, we can conclude that the presence of the radial gradient seems confirmed in this field. Indeed, if thick disk stars are as metal poor we as we have drawn them in the figure, then the mean bulge IDF is $\langle$[Fe/H]$\rangle = -0.26$, lower than in the innermost fields. Even if thick disk stars are more metal rich, regardless of how many they are, then the mean metallicity of the remaining bulge stars can only be even lower.

The discussion above draws our attention to the fact that our knowledge of the disk properties, far away from the Sun, is still extremely poor. The Besançon model predicts a large amount of thick disk stars in the central region of our Galaxy. However, there is certainly a hole in the HI and CO distribution inside ∼3 kpc (e.g., Dame et al. 2001), and we know that in most barred galaxies disk stars are *cleaned up* in the central region. The Besançon model does include a central hole in the thin disk distribution, but its thick disk has a pure exponential radial distribution. Does the real thick disk follow the thin disk and gas distribution, or does it keep growing toward the center?

On one hand, this emphasizes the importance of gathering more information about the inner disk, in order to understand not only the properties of the disk itself but also of other galactic components affected by disk contamination. On the other hand, the lower panel of Fig. 14, if hard to interpret in terms of bulge IDF, poses already important constraints on the properties of the inner disk. Namely, if as much as 60% of the observed stars at $b = -12°$ belong to the thick disk, then their metallicity *must* be definitely higher than it is in the solar neighborhood, and possibly also much narrower.

Finally, we note that while we found indications of a radial gradient between $b = -4°$ and $b = -12°$, the results by Rich et al. (2007) indicate a flattening between $(l, b) = (1, -4)$ and $(l, b) = (0, -1)$. A flattening of the radial gradient in the inner bulge below $b = -4°$ was also obtained by Ramírez et al. (2000) from low resolution spectroscopy of giant stars. Also Tyson & Rich (1993) using Washington photometry found a radial gradient outside $b = -6°$ and a flattening (or a slight turnover) in the inner part.

9. Metallicity versus kinematics

Figure 15 shows the radial velocities versus metallicity for bulge field stars in the three fields. A couple of important pieces of information can be extracted from such a plot.

First, as expected, the velocity dispersion goes down along the bulge minor axis, being $\sigma_{RV} = 105$ km s^{-1} in Baade's Window, $\sigma_{RV} = 84$ km s^{-1} in the $b = -6°$ field, and $\sigma_{RV} = 80$ km s^{-1} in the field at $b = -12°$. The latter would be further reduced to $\sigma_{RV} = 60$ km s^{-1} if the 5 stars with absolute velocity $|V_{RV}| > 150$ km s^{-1} are rejected (e.g., if they were halo stars).

Second, the velocity dispersion of the metal rich tail is extremely different in the three fields along the minor axis, being hotter than the metal-poor one in the innermost field, about the same in the intermediate one, and extremely cold in the outermost field. The latter field being heavily contaminated by disk stars, we are inclined to think that the metal rich tail is in fact made by thin disk stars (see discussion at the end of Sect. 7). On the contrary, since the two innermost fields both have negligible disk contamination, the interpretation of such a different kinematical behaviour of the metal rich component with respect to the metal poor one is not at all straightforward. A detailed analysis of the bulge kinematics from the present data will be presented in Babusiaux et al. (2008, in preparation).

10. Discussion and conclusions

Figure 16 shows the [Fe/H] distribution in the Baade's Window field with superimposed the distribution function of a simple, one-zone, closed-box model of chemical evolution with an assumed iron yield $y_{Fe} = +0.03$. The simple model has been normalized to 1, plotting the fraction of the total number of stars at each metallicity, as for the observed distribution. Rich (1990)

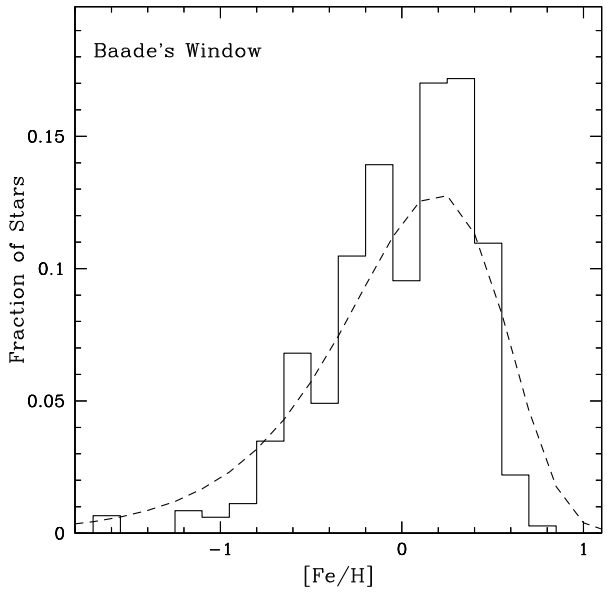

Fig. 16. The observed bulge IDF in Baade's Window compared with a simple, one-zone model with an assumed iron yield of $y_{\rm Fe} = +0.03$.

first noted that such simple chemical evolution model is a fairly good match to the bulge data, in his case the Rich (1988) data. As shown in Fig. 16, this is still the case for the data presented in this paper. However, at a closer look the match does not look perfect: the observed distribution appears to be a little narrower than the model one, and would be even narrower after deconvolving it for the observational errors. Moreover, the observed distribution shows a sharper cutoff at high metallicity, compared with the closed box model. A small deficit at the low-metallicity end with respect to the model was noticed by Zoccali et al. (2003) for their photometric IDF. A small deficit was also found by Fulbright et al. (2006) for the original Rich (1988) sample of bulge K giants, having recalibrated the old data using Keck/HIRES high resolution spectra for a subsample of the stars. But overall, they find quite good agreement with a closed-box model, once either the mean or the median iron abundance is used for the yield.

Undoubtedly, a closed-box model provides a rather satisfactory *qualitative* match to the data. Should we conclude that the bulge really evolved as a closed box? Certainly not. In such a model the bulge starts its evolution with its whole mass in gaseous form, and proceeds with star formation till gas exhaustion. Thus, the closed-box model describes the chemical evolution of the classic *monolithic collapse* model. In modern scenarios for the bulge formation, via either merging of smaller entities or via disk instabilities, the bulge is assembled gradually, rather than being already in one piece from the beginning. Thus, the bulge "box" was open with respect to gas (and stars) accretion. Moreover, most likely it was also open in the opposite direction, i.e., ejecting gas and metals via supernova/AGN driven winds. We expand here on this latter aspect.

The iron yield from theoretical stellar nucleosynthesis is subject to large uncertainties, which are difficult to reduce without help from observations. The iron yield from individual massive stars exploding as type II supernovae is critically dependent upon the precise location of the *mass cut* between the compact remnant and the supernova ejecta, which in fact cannot be reliably predicted. In the case of type Ia supernovae (SNIa), it is their total number (and their distribution of delay times) as a result of turning a given amount of gas into stars that can hardly be predicted only from first principles (e.g., Greggio 2005). For these reasons, an empirical estimate of the iron yield may be especially helpful. Such an opportunity can be exploited in the case of clusters of galaxies, which indeed are more likely to have retained all the stars, gas and metals that have participated in the evolution. Thus, combining the iron content of the intracluster medium from X-ray observations, with that in stars from optical observations of cluster galaxies, one finds that clusters contain ∼0.015 $M_\odot$ of iron for each B-band solar luminosity of the cluster galaxies (Renzini 1997, 2004). We shall now explore the consequences of assuming that this empirical iron yield applies also to the Milky Way bulge.

Most of the iron in clusters of galaxies was produced by the dominant stellar population, i.e. by stars in early-type galaxies that formed at $z \gtrsim 2$ (for a review, see Renzini 2006), i.e., by galactic spheroids. With an age of over ∼10 Gyr (Zoccali et al. 2003), also the stars in the bulge "formed at $z \gtrsim 2$", and the bulge is a spheroid. Thus, our assumption of a similar iron yield in the bulge as in clusters is quite reasonable. Now, with a present B-band luminosity of $\sim 6 \times 10^9\ L_{\rm B,\odot}$ (Kent et al. 1991), the bulge stellar population should have produced $\sim 6 \times 10^9 \times 0.015 = 9 \times 10^7\ M_\odot$ of iron. But with a mass of $1.6 \times 10^{10}\ M_\odot$ (e.g., Han & Gould 1995; Bissantz & Gerhard 2002; Sumi et al. 2006) and a mean iron abundance (in mass) $\langle Z_{\rm Fe} \rangle = 0.0018$ (as the average of the individual $Z_{\rm Fe} = Z_{\rm Fe,\odot} \times 10^{\rm [Fe/H]}$ in Baade's Window) the bulge contains today only $\sim 2.9 \times 10^7\ M_\odot$ of iron, i.e., about a factor of 3 less than it should have produced. Therefore, under this assumption the bulge would have ejected ∼70% of the iron it had produced (Renzini 2004).

Chemical evolution models for the bulge that relax the closed-box approximation not only with regard to bulge assembly (as in e.g., Matteucci et al. 1999), but also allowing for bulge winds are now appearing in the literature (Ferreras et al. 2003; Ballero et al. 2007; Tsujimoto 2007). The bulge IDF predicted by Ballero et al. (2007) qualitatively agrees with the one measured here (cf., their Fig. 3). However, these models involve several free parameters, which are needed to describe the rate at which new gas (and stars) are added to the growing bulge, the star formation law, the IMF, the stellar nucleosynthesis, the distribution of delay times for SNIa's, and the onset and strengths of the winds. Some of these parameters produce similar changes on the predicted IDF making the comparison between observed and model IDF not sufficient to constrain the whole formation scenario. In addition, the models predict a *global* IDF for the whole bulge. Due to the presence of a radial metallicity gradient, a direct comparison with observations is not straightforward. In view of these difficulties, it is worth summarizing here what are the major, purely observational constraints on the formation and evolution of the Galactic bulge.

Zoccali et al. (2003) have shown that a simulated CMD with an age of 13 Gyr (that includes the bulge metallicity distribution) gives a fairly good match to the bulge CMD. In particular, this good match includes the luminosity difference between the horizontal branch and the main sequence turnoff, a classical age indicator. However, due to metallicity, reddening, and distance dispersion, the bulge turnoff cannot be located to better than 0.2−0.3 mag, corresponding to an age uncertainty of ∼2−3 Gyr. Conservatively, we take the age of the bulk of bulge stars to be in excess of 10 Gyr, and even so this implies that star formation and chemical enrichment had to be confined within a time interval definitely shorter than the age of the universe at a lookback time of 10 Gyr, or ≲3.7 Gyr according to the current concordance cosmology. If the bulk of bulge stars formed in the cosmic time interval corresponding to redshift between 3 and 2, then star formation cannot have taken much more than ∼1 Gyr.

Thus, the main uncertainty affecting the duration of the star formation in the bulge comes from the uncertainty in its age: the older the age, the shorter the star-formation era.

The second constraint on the formation timescale of the bulge comes from the observed α-element enhancement (McWilliam & Rich 1994, 2003; Barbuy et al. 2006; Zoccali et al. 2004, 2006; Lecureur et al. 2007; Fulbright et al. 2007), once this is interpreted as a result of the interplay of the fast delivery of iron-poor nucleosynthesis products of massive stars by SNII's, with the slow delivery of iron-rich products by SNIa's. Again, a star formation timescale of approximately 1 Gyr is generally derived from chemical evolution models, which typically assume a distribution of SNIa delay times from Greggio & Renzini (1983). Thus, the derived timescale is modulo the adopted distribution of SNIa delay times. Other equally plausible distributions (e.g. Greggio 2005) would have given shorter or longer timescales. Thus, until the actual mix of SNIa progenitors is fully identified, we shall remain with this uncertainty on how to translate an α-element overabundance into a star formation timescale. All in all, combining the age and the α-element enhancement constraints, it is fair to conclude that the formation of the bulge cannot have taken much more that ~1 Gyr, and possibly somewhat less than that.

In addition, the indications of a radial metallicity gradient found here would argue against the formation via secular evolution of the bar, because obviously the vertical heating that transforms a bar into a *pseudo*-bulge would not act preferentially on metal poor stars. However, combining our result with previous ones on the inner bulge, at the moment there is evidence of a flat metallicity distribution inside ~600 pc, and a radial gradient outside. Should those findings be confirmed, they might indicate the presence of a double-component bulge, an inner *pseudo*-bulge, and an outer classical one, as already found by Peletier et al. (2007) within the SAURON survey of galaxy bulges.

Finally, concerning the bulge chemical evolution, from the IDF we can certainly conclude that the bulge must have accreted primordial gas, due to the lack of metal poor stars with respect to the simple model prediction (the so-called G dwarf problem, solved with the inclusion of some infall in the model) and must have ejected a substantial fraction of the iron it produced (outflow). In addition, from the overabundance of α-elements quoted above we can conclude that it cannot have accreted stars already significantly enriched by SNIa products, such as disk stars, or stars born in small galactic entities similar to the surviving satellite galaxies in the Local Group (e.g., Venn et al. 2004).

Acknowledgements. We thank Yazan Momany for providing the astrometric and photometric catalogue for the NGC 6553 field. We thank Mathias Schultheis for providing us the results of an updated version of the Besançon Galaxy model. This work has been partly funded by the FONDAP Center for Astrophysics 15010003 (M.Z. and D.M.) and by Projecto FONDECYT Regular #1085278. D.M. and B.B. acknowledge the European Commission's ALFA-II programme, through its funding of the Latin-american European Network for Astrophysics and Cosmology (LENAC). B.B. acknowledges grants from CNPq and Fapesp. S.O. acknowledges the Italian Ministero dell'Università e della Ricerca Scientifica e Tecnologica (MURST) under the program 'Fasi iniziali di evoluzione dell'alone e del bulge Galattico' (Italy).

References

Alcock, C., Allsman, R. A., Alves, D. R., et al. 1998, ApJ, 492, 190
Alonso, A., Arribas, S., & Martínez-Roger, C. 1999, A&AS, 140, 261
Alvarez, R., & Plez, B. 1998, A&A, 330, 1109
Bagnulo, S., Jehin, E., Ledoux, C., et al. 2003, Messenger, 114, 10
Ballero, S. K., Matteucci, F., Origlia, L., & Rich, R. M. 2007, A&A, 467, 123
Barbuy, B., Perrin, M.-N., Katz, D., et al. 2003, A&A, 404, 661
Barbuy, B., Zoccali, M., Hill, V., et al. 2006, ESO Astrophys. Symp., ed. S. Randich, & L. Pasquini, 87
Barbuy, B., Zoccali, M., Ortolani, S., et al. 2007, AJ, 134, 1613
Barklem, P. S., Anstee, S. D., & O'Mara, B. J. 1998, PASA, 15, 336
Barklem, P. S., Piskunov, N. E., & O'Mara, B. J. 2000, A&AS, 142, 467
Blecha, A., North, P., Royer, F., & Simond, G. 2003, BLDR Software Reference Manual 1.09, VLT-SPE-OGL-13730-0040, http://www.eso.org/instruments/flames/manuals.html
Bissantz, N., & Gerhard, O. 2002, MNRAS, 330, 591
Busso, G., Moehler, S., Zoccali, M., Heber, U., & Yi, S. K. 2005, ApJ, 633, L29
Carpenter, J. M. 2001, AJ, 121, 2851
Cavallo, R. M., Cook, K. H., Minniti, D., & Vanderhei, T. 2003, in Discoveries and Research Prospects from 6- to 10-Meter-Class Telescopes II, ed. P. Guhathakurta, Proc. SPIE, 4834, 66 [arXiv:astro-ph/0209196]
Coelho, P., Barbuy, B., Meléndez, J., Schiavon, R. P., & Castilho, B. V. 2005, A&A, 443, 735
Cohen, J. G., Huang, W., Udalski, A., Gould, A., & Johnson, J. 2008, AJ, submitted [arXiv:0801.3264]
Collinge, M. J., Sumi, T., & Fabrycky, D. 2006, ApJ, 651, 197
Dame, T. M., Hartman, D., & Thaddeus, P. 2001, ApJ, 547, 792
Feltzing, F., & Gilmore, G. 2000, A&A, 355, 949
Ferreras, I., Wyse, R. F. G., & Silk, J. 2003, MNRAS, 345, 1381
Fuhr, J. R., & Wiese, W. L. 2006, JPCRD, 35, 1669
Fulbright, J. P., McWilliam, A., & Rich, R. M. 2006, ApJ, 636, 821
Fulbright, J. P., McWilliam, A., & Rich, R. M. 2007, ApJ, 661, 1152
Gratton, R. G., & Sneden, C. 1990, A&A, 234, 366
Greggio, L. 2005, A&A, 441, 1055
Greggio, L., & Renzini, A. 1983, A&A, 118, 217
Gustafsson, B., Edvardsson, B., Eriksson, K., et al. 2002, in Stellar Atmosphere Modeling, ed. I. Hubeny, D. Mihalas, & K. Werner, ASP Conf. Ser., 288, 331
Han, C., & Gould, A. 1995, ApJ, 449, 521
Ibata, R. A., & Gilmore, G. 1995a, MNRAS, 275, 591
Ibata, R. A., & Gilmore, G. 1995b, MNRAS, 275, 605
Johnson, A. J., Gal-Yam, A., Leonard, D. C., et al. 2007, ApJ, 655, L33
Johnson, A. J., Gaudi, B. S., Sumi, T., Bond, I. A., & Gould, A. 2008, AJ, submitted [arXiv:0801.2159]
Kent, S. M., Dame, T. M., & Fazio, G. 1991, ApJ, 378, 131
Kormendy, J., & Kennicutt, R. C. Jr. 2004, ARA&A, 42, 603
Kuijken, K., & Rich, R. M. 2002, AJ, 123, 2054
Lecureur, A., Hill, V., Zoccali, M., et al. 2007, A&A, 465, 799
Lecureur, A., Hill, V., Zoccali, M., et al. 2008, A&A, in preparation
Magain, P. 1984, A&A, 134, 189
Martin, W. C., et al. 2002, NIST Atomic Database, version 2.0 (Gaithersburg, MD: National Institute of Standards and Technology), http://physics.nist.gov/asd
Matteucci, F., Romano, D., & Molaro, P. 1999, A&A, 341, 458
Minniti, D. 1996, ApJ, 459, 175
Momany, Y., Vandame, B., Zaggia, S., et al. 2001, A&A, 379, 436
McWilliam, A., & Rich, R. M. 1994, ApJ, 91, 749
McWilliam, A., & Rich, R. M. 2003, in Origin and Evolution of the Elements (http://www.ociw.edu/ociw/symposia/series/symposium4/proceedings.html)
Nordström, B., Mayor, M., Andersen, J., et al. 2004, A&A, 418, 989
Ortolani, S., Renzini, A., Gilmozzi, R., et al. 1995, Nature, 377, 701
Pasquini, L., Alonso, J., Avila, G., et al. 2003, SPIE, 484, 1682
Peletier, R. F., Falco'n-Barroso, J., Bacon, R., et al. 2007, MNRAS, 379, 445
Ramírez, I., & Meléndez, J. 2005, ApJ, 626, 465
Ramírez, S. V., Stephens, A. W., Frogel, J. A., & DePoy, D. L. 2000, AJ, 120, 833
Reddy, B. E., Lambert, D. L., & Allende Prieto, C. 2006, MNRAS, 367, 1329
Renzini, A. 1997, ApJ, 488, 35
Renzini, A. 2004, in Clusters of Galaxies, ed. J. S. Mulchaey, A. Dressler, & A. Oemler (Cambridge, CUO), 16
Renzini, A. 2006, ARA&A, 44, 141
Rich, R. M. 1988, AJ, 95, 828
Rich, R. M. 1990, ApJ, 362, 604
Rich, R. M., & Origlia, L. 2005, ApJ, 634, 1293
Rich, R. M., Origlia, L., & Valenti, E. 2007, ApJ, 665, L119
Robin, A. C., Reylé, C., Derrière, S., & Picaud, S. 2003, A&A, 409, 523
Sadler, E. M., Rich, R. M., & Terndrup, D. M. 1996, AJ, 112, 171
Spite, M. 1967, Annales d'Astroph., 30, 211
Sumi, T., Woźniak, P. R., Udalski, A., et al. 2006, ApJ, 636, 240
Tsujimoto, T. 2007, ApJ, 665, L115
Tyson, N. D., & Rich, R. M. 1993, in Galactic Bulges, ed. DeJonghe, & Habing (Dordrecht: Kluwer), IAU Symp., 153, 333
Udalski, A., Szymanski, M., Kubiak, M., et al. 2002, Acta Astron., 52, 217
Venn, K. A., Irwin, M., Shetrone, M. D., et al. 2004, AJ, 128, 1177
Zoccali, M., Renzini, A., Ortolani, S., et al. 2003, A&A, 399, 931
Zoccali, M., Barbuy, B., Hill, V., et al. 2004, A&A, 423, 507
Zoccali, M., Lecureur, A., Barbuy, B., et al. 2006, A&A, 457, L1

Table 3. Stellar parameters and iron abundance of all the program stars.

QF[a]	ID	OGLE-ID	RA	Dec	V	$V-I$	$\log g$	V_t	$T_{\rm eff}$	[Fe/H]	σ^b	Cluster?
Baade's window												
0	2	423342	18:03:50.00	–29:55:45.20	16.36	1.805	1.99	1.3	4650	0.46	0.38	–
0	3	423323	18:03:48.39	–29:56:27.10	16.10	1.846	1.59	1.5	4200	–0.48	0.18	–
0	4	412779	18:03:43.18	–29:59:40.10	15.91	1.667	1.93	1.5	4850	–0.37	0.18	–
2	5	412803	18:03:46.14	–29:58:30.00	16.40	2.083	1.52	1.3	4000	0.51	0.34	–
0	6	423359	18:03:47.03	–29:54:49.20	16.17	1.768	1.92	1.4	4650	–1.23	0.23	–
2	7	433669	18:03:37.14	–29:54:22.30	16.14	1.854	1.67	1.5	4300	0.54	0.37	–
0	8	412752	18:03:46.04	–30:00:50.90	15.99	1.606	1.98	1.5	4900	–0.80	0.15	NGC 6522
0	9	412794	18:03:44.84	–29:58:51.40	16.31	1.823	1.94	1.3	4600	0.13	0.25	–
0	11	402327	18:03:49.92	–30:03:35.30	16.15	1.691	2.00	1.2	4800	0.15	0.21	–
1	14	412924	18:03:47.33	–29:59:48.30	16.29	1.660	2.05	1.5	4800	0.48	0.34	–
0	15	575317	18:04:01.48	–29:56:23.60	15.98	1.677	1.78	1.4	4550	0.22	0.26	–
1	16	92600	18:04:07.46	–29:54:59.70	16.29	2.050	1.70	1.0	4250	0.05	0.30	–
0	17	412759	18:03:47.35	–30:00:36.40	15.97	1.649	1.98	1.4	4900	–0.39	0.11	–
2	21	575356	18:03:54.82	–29:55:10.40	16.38	2.065	1.56	1.4	4050	0.39	0.35	–
0	22	423331	18:03:51.67	–29:56:17.60	16.31	1.854	1.88	1.5	4500	0.18	0.25	–
1	24	564797	18:04:03.20	–29:58:59.60	16.37	2.025	1.69	1.5	4200	0.24	0.29	–
0	25	564792	18:04:06.45	–29:59:13.70	16.11	1.631	2.09	1.4	5000	–0.68	0.21	–
0	26	412931	18:03:51.32	–29:59:43.10	16.36	1.867	1.87	1.3	4450	–0.15	0.20	–
0	27	564988	18:03:53.94	–29:59:29.90	16.33	1.751	2.04	1.4	4750	–0.24	0.18	–
0	30	412792	18:03:47.65	–29:58:55.10	16.27	1.859	1.83	1.4	4450	–0.26	0.18	–
0	31	564762	18:03:53.30	–30:00:26.50	15.98	1.728	1.87	1.6	4700	–0.63	0.12	–
0	33	564757	18:04:05.96	–30:00:43.90	16.18	1.627	2.01	1.3	4800	0.38	0.22	–
0	35	564807	18:04:00.26	–29:58:24.80	16.09	1.690	2.00	1.5	4850	–0.67	0.15	–
0	37	575293	18:04:04.43	–29:57:16.30	16.34	1.842	1.79	1.3	4450	0.41	0.43	–
0	38	92537	18:04:18.99	–29:57:52.60	16.13	1.864	1.81	1.3	4500	–0.56	0.13	–
0	39	575303	18:04:04.81	–29:56:55.20	16.14	1.580	2.02	1.5	4850	–0.27	0.14	–
0	40	240260	18:04:39.62	–29:55:19.80	15.88	1.601	2.07	1.4	5150	–0.26	0.14	–
0	41	82762	18:04:20.52	–29:58:13.10	16.21	1.769	1.81	1.4	4450	0.31	0.28	–
0	42	92565	18:04:17.20	–29:56:49.10	16.38	2.081	1.84	1.5	4400	–0.05	0.22	–
0	43	240210	18:04:28.97	–29:57:36.70	16.16	1.782	2.00	1.2	4800	–0.04	0.22	–
0	44	554722	18:04:03.71	–30:01:33.00	16.12	1.811	1.67	1.6	4600	–0.44	0.14	–
0	45	82725	18:04:10.12	–29:59:45.80	16.19	1.673	1.98	1.3	4750	–0.70	0.16	–
0	46	231262	18:04:33.97	–29:59:54.30	16.29	1.636	2.04	1.4	4930	–0.10	0.18	–
0	47	231099	18:04:27.24	–30:01:10.30	15.90	1.527	2.06	1.6	5100	–0.22	0.13	–
0	48	82747	18:04:09.88	–29:58:51.80	16.03	1.656	2.06	1.3	5000	–0.26	0.16	–
0	49	63856	18:04:11.16	–30:05:18.70	16.33	1.814	2.01	1.3	4700	0.33	0.26	–
0	50	231144	18:04:27.23	–29:58:56.50	16.15	1.793	1.94	1.5	4700	–0.20	0.18	–
0	53	231364	18:04:34.47	–29:58:24.70	16.14	1.693	1.99	1.5	4800	0.27	0.25	–
1	54	82742	18:04:13.80	–29:59:13.40	15.98	1.746	1.68	1.5	4400	0.17	0.31	–
1	55	73506	18:04:08.81	–30:02:03.30	16.32	2.036	1.67	1.5	4200	–0.24	0.25	–
0	56	222451	18:04:23.77	–30:02:23.50	16.08	1.759	1.94	1.3	4750	–0.33	0.20	–
0	57	73504	18:04:08.02	–30:02:16.40	16.33	1.957	1.92	1.4	4550	–0.16	0.19	–
0	58	82761	18:04:16.23	–29:58:16.30	16.18	1.755	2.01	1.5	4800	–0.21	0.15	–
1	59	73490	18:04:11.50	–30:02:56.10	16.31	1.984	1.74	1.2	4300	0.49	0.37	–
0	60	222618	18:04:33.22	–30:02:11.70	16.23	1.825	2.03	1.4	4800	–0.33	0.19	–
2	61	357480	18:04:43.92	–30:03:15.20	16.31	1.796	2.06	1.4	4800	0.32	0.37	–
0	62	554664	18:04:05.38	–30:04:09.30	16.22	1.927	1.91	1.5	4600	–0.48	0.17	–
0	64	73514	18:04:09.99	–30:01:42.40	16.13	1.705	2.04	1.5	4900	–0.41	0.18	–
2	65	205243	18:04:35.02	–30:10:55.30	16.34	1.903	2.13	1.4	4900	0.31	0.41	–
0	66	82705	18:04:14.25	–30:01:11.20	16.10	1.883	1.80	1.4	4500	–0.19	0.19	–
1	68	205257	18:04:31.86	–30:10:09.90	16.23	1.813	1.94	1.5	4600	–1.10	0.26	–
0	69	82831	18:04:18.85	–30:00:35.80	16.19	1.673	1.99	1.4	4750	0.33	0.27	–
0	71	205436	18:04:28.84	–30:08:58.10	16.30	1.662	2.27	1.4	5200	0.16	0.20	–
0	72	82798	18:04:10.78	–30:01:10.00	16.25	1.593	2.17	1.1	5050	–0.06	0.17	–
0	73	73515	18:04:15.53	–30:01:42.60	16.05	1.814	1.81	1.4	4550	–0.45	0.15	–
1	74	214035	18:04:23.37	–30:06:30.60	16.17	1.803	1.92	1.4	4650	0.26	0.42	–
0	76	63794	18:04:14.65	–30:08:38.50	16.22	1.868	2.00	1.3	4750	–0.31	0.22	–
0	77	63792	18:04:19.86	–30:08:40.80	16.23	1.917	1.82	1.3	4450	–0.15	0.22	–
0	78	54167	18:04:14.82	–30:11:45.40	16.30	1.685	2.06	1.4	4800	–0.38	0.23	–
2	79	54104	18:04:20.20	–30:09:59.00	16.39	1.976	1.95	1.5	4550	–0.28	0.36	–

Table 3. continued.

QF[a]	ID	OGLE-ID	RA	Dec	V	$V-I$	$\log g$	V_t	$T_{\rm eff}$	[Fe/H]	σ^b	Cluster?
0	80	54132	18:04:21.69	–30:08:55.90	16.11	1.677	2.06	1.4	4950	–0.11	0.23	–
1	81	54273	18:04:14.72	–30:10:15.80	16.39	1.700	2.12	1.3	4850	0.45	0.34	–
0	82	44560	18:04:23.04	–30:12:45.30	16.35	1.904	1.93	1.4	4550	–0.23	0.23	–
0	83	205356	18:04:24.17	–30:10:35.30	16.36	1.700	2.16	1.5	4950	–0.19	0.24	–
0	85	63800	18:04:09.87	–30:08:21.70	15.99	1.667	1.96	1.5	4850	0.31	0.25	–
0	86	63849	18:04:07.60	–30:05:42.10	16.16	1.784	1.97	1.4	4750	–0.92	0.19	–
1	87	537070	18:04:01.40	–30:10:20.70	16.07	1.693	2.14	1.1	5150	–1.03	0.16	–
0	88	63823	18:04:14.08	–30:07:31.10	16.19	1.925	1.87	1.4	4550	–0.04	0.20	–
0	90	545401	18:03:54.55	–30:06:35.50	16.23	1.629	2.22	1.4	5150	0.01	0.19	–
0	91	545440	18:03:59.36	–30:06:02.20	16.38	1.931	1.91	1.5	4500	–0.60	0.18	–
0	92	54311	18:04:12.68	–30:09:40.70	16.39	1.697	2.15	1.5	4900	0.26	0.24	–
0	93	537101	18:04:05.17	–30:09:53.80	16.34	1.876	2.07	1.3	4800	–0.67	0.18	–
0	95	554655	18:04:02.54	–30:04:31.00	16.10	1.782	2.03	1.5	4900	–0.34	0.17	–
0	96	392918	18:03:36.89	–30:07:04.30	16.37	2.017	1.97	1.4	4600	0.05	0.24	–
0	97	63839	18:04:11.86	–30:06:20.80	16.29	2.072	1.74	1.4	4300	–0.22	0.29	–
0	98	554700	18:03:58.14	–30:02:33.50	16.07	1.637	2.02	1.4	4900	–0.17	0.17	–
0	99	554787	18:04:00.20	–30:04:06.70	16.39	1.754	2.04	1.2	4700	–0.58	0.16	–
0	100	63855	18:04:16.04	–30:05:25.00	16.33	2.029	1.67	1.4	4200	0.40	0.28	–
1	101	63850	18:04:18.50	–30:05:40.30	15.91	1.659	1.78	1.6	4600	–1.61	0.18	–
0	102	402294	18:03:51.01	–30:04:48.60	16.29	1.761	2.05	1.2	4800	–0.50	0.18	–
0	103	63820	18:04:07.86	–30:07:35.00	16.22	1.679	2.19	1.2	5100	–0.14	0.20	–
0	104	393015	18:03:52.55	–30:07:31.20	16.31	1.775	2.09	1.3	4850	–0.06	0.17	–
0	105	554663	18:03:57.10	–30:04:13.10	15.95	1.738	1.86	1.3	4700	–0.72	0.14	–
0	106	63834	18:04:14.43	–30:06:46.70	16.14	1.802	2.08	1.4	4950	0.16	0.19	–
2	107	402361	18:03:36.59	–30:02:16.10	15.98	1.664	2.00	1.4	4950	–1.05	0.21	NGC 6522
1	109	402307	18:03:42.86	–30:04:06.90	16.28	1.835	1.93	1.5	4600	0.40	0.32	–
0	110	402414	18:03:40.91	–30:04:41.80	16.35	1.858	1.99	1.4	4650	–0.21	0.26	–
1	111	545288	18:04:02.82	–30:05:06.00	16.31	1.791	1.94	1.3	4600	0.13	0.27	–
0	112	554889	18:04:03.56	–30:02:34.00	16.33	1.638	2.18	1.3	5000	–0.10	0.18	–
0	113	402315	18:03:40.66	–30:03:50.20	16.14	1.862	1.97	1.4	4750	–0.17	0.17	–
0	114	554811	18:03:55.78	–30:03:48.80	16.30	1.659	2.11	1.3	4900	0.17	0.18	–
0	115	234671	18:03:34.49	–30:07:01.40	16.27	1.976	1.86	1.4	4500	0.06	0.29	–
0	117	402332	18:03:41.82	–30:03:24.30	16.16	1.886	1.82	1.4	4500	–0.31	0.19	–
1	118	402322	18:03:42.24	–30:03:39.90	16.01	1.701	1.94	1.5	4800	–0.94	0.17	NGC 6522
0	119	564743	18:04:00.41	–30:01:12.00	16.30	1.955	1.70	1.4	4250	0.21	0.31	–
0	120	402311	18:03:37.88	–30:03:58.70	16.34	1.888	1.89	1.5	4500	0.08	0.25	–
1	122	244582	18:03:33.34	–30:01:58.30	16.00	1.720	2.01	1.3	4950	–0.81	0.14	NGC 6522
0	123	244504	18:03:27.60	–30:04:29.40	16.10	1.877	1.83	1.4	4550	–0.25	0.21	–
0	128	402607	18:03:44.61	–30:02:10.40	16.26	1.707	2.04	1.3	4800	–0.82	0.17	NGC 6522
1	130	402531	18:03:41.00	–30:03:03.00	16.30	1.660	2.21	1.2	5100	–0.85	0.17	NGC 6522
0	132	402325	18:03:49.04	–30:03:38.20	16.27	1.876	1.87	1.4	4500	–0.32	0.17	–
0	135	256308	18:03:35.49	–30:00:05.30	16.06	1.623	1.95	1.4	4800	–1.69	0.20	–
0	3	585982	18:03:53.07	–29:53:30.50	16.43	1.903	1.99	1.4	4600	–0.08	0.26	–
1	4	575308	18:03:56.30	–29:56:40.60	16.47	2.255	1.84	1.4	4350	0.27	0.40	–
0	5	575289	18:03:56.86	–29:57:26.20	16.48	1.963	1.92	1.5	4450	–0.50	0.24	–
2	7	423298	18:03:51.29	–29:57:27.90	16.54	2.192	1.91	1.2	4400	–0.08	0.31	–
1	8	433830	18:03:41.76	–29:53:17.60	16.82	2.187	1.87	1.5	4200	0.17	0.43	–
1	9	564963	18:03:59.09	–29:59:46.20	16.62	1.971	1.83	1.0	4250	0.34	0.42	–
0	10	554980	18:04:02.87	–30:01:29.20	16.42	1.726	1.99	1.5	4600	0.31	0.39	–
2	13	423304	18:03:43.75	–29:57:15.90	16.95	2.296	2.03	1.4	4350	0.22	0.42	–
2	14	102833	18:04:14.55	–29:51:36.90	16.75	2.108	2.05	1.5	4500	0.29	0.37	–
1	15	102853	18:04:11.78	–29:51:09.50	16.43	2.028	1.86	1.2	4400	0.15	0.39	–
0	16	564768	18:04:05.90	–29:59:53.10	16.59	2.186	1.74	1.3	4150	–0.30	0.26	–
0	17	586077	18:04:06.36	–29:53:53.20	16.66	2.002	2.02	1.3	4500	0.21	0.28	–
1	18	586005	18:04:04.92	–29:52:42.30	16.55	2.133	1.91	1.3	4400	0.29	0.42	–
0	19	564789	18:04:03.96	–29:59:21.90	16.60	2.255	1.70	1.2	4100	–0.15	0.28	–
2	20	596502	18:03:59.27	–29:49:51.50	16.94	2.520	1.87	1.1	4150	0.28	0.50	–
1	21	575360	18:04:00.11	–29:55:07.30	16.56	2.077	1.96	1.2	4500	–0.05	0.37	–
1	22	564991	18:04:02.46	–29:59:28.90	16.73	2.117	1.98	1.4	4400	0.19	0.34	–
2	26	82760	18:04:13.27	–29:58:17.80	16.64	2.192	1.87	1.5	4300	0.25	0.41	–
1	28	82727	18:04:08.96	–29:59:41.20	16.59	2.234	1.78	1.3	4200	0.17	0.35	–
0	29	92557	18:04:12.49	–29:57:16.00	16.43	1.888	2.05	1.4	4700	–0.07	0.27	–
2	33	231128	18:04:31.51	–29:59:51.80	16.55	2.338	1.76	1.4	4200	0.17	0.45	–

Table 3. continued.

QF[a]	ID	OGLE-ID	RA	Dec	V	$V-I$	$\log g$	V_t	$T_{\rm eff}$	[Fe/H]	σ^b	Cluster?
0	34	82717	18:04:17.68	–30:00:29.70	16.57	2.286	1.77	1.1	4150	0.28	0.39	–
1	35	240216	18:04:26.41	–29:57:16.50	16.42	1.968	1.86	1.2	4400	0.19	0.39	–
0	36	240459	18:04:33.58	–29:54:49.40	16.57	1.880	2.02	1.2	4550	–0.39	0.25	–
1	37	240394	18:04:34.29	–29:55:54.40	16.56	1.960	2.04	1.6	4600	0.14	0.30	–
1	38	231369	18:04:33.83	–29:58:19.60	16.71	2.112	1.82	1.5	4200	0.29	0.39	–
0	40	231367	18:04:26.86	–29:58:20.80	16.45	1.849	2.00	1.4	4600	–0.01	0.25	–
1	41	231310	18:04:33.50	–29:59:12.50	16.50	1.924	1.95	1.1	4500	0.30	0.38	–
1	42	374186	18:04:41.73	–29:55:17.60	16.76	2.142	1.96	1.2	4350	0.20	0.36	–
1	43	231325	18:04:24.08	–29:59:00.60	16.69	2.078	1.81	1.5	4200	0.34	0.36	–
0	46	222627	18:04:25.51	–30:01:60.00	16.81	2.270	1.78	1.1	4100	0.13	0.38	–
0	49	231185	18:04:33.44	–30:01:12.90	16.57	1.997	1.98	1.3	4500	0.19	0.32	–
2	51	231233	18:04:34.84	–30:00:26.40	16.45	1.819	1.97	1.3	4550	–0.16	0.28	–
0	53	365797	18:04:54.55	–29:58:16.40	16.40	2.017	1.95	1.3	4550	–0.19	0.25	–
0	54	222412	18:04:29.91	–30:04:32.00	16.42	2.074	1.86	1.3	4400	–0.11	0.21	–
1	55	222408	18:04:29.73	–30:04:49.60	16.65	2.182	1.72	1.5	4100	0.31	0.36	–
1	56	357466	18:04:55.47	–30:03:28.00	16.92	2.435	1.98	1.3	4300	0.43	0.44	–
0	57	350527	18:04:47.62	–30:05:14.10	16.55	2.234	2.04	1.4	4600	–0.65	0.16	–
0	59	222523	18:04:32.75	–30:03:53.10	16.74	2.191	1.88	1.4	4250	0.01	0.34	–
1	60	222543	18:04:38.20	–30:03:24.50	16.85	2.452	1.99	1.1	4350	0.34	0.41	–
0	61	357436	18:04:40.16	–30:03:53.10	16.50	1.913	1.95	1.3	4500	0.44	0.42	–
0	62	357459	18:04:47.78	–30:03:32.10	16.64	2.008	2.08	1.5	4600	–0.01	0.29	NGC 6528
0	64	73607	18:04:13.37	–30:03:40.10	16.44	1.772	2.00	1.2	4600	0.28	0.40	–
0	65	73483	18:04:10.39	–30:03:21.30	16.63	2.142	1.87	1.4	4300	0.16	0.33	–
1	66	73609	18:04:14.37	–30:03:35.30	16.73	2.210	1.91	1.5	4300	0.28	0.49	–
0	67	214192	18:04:23.95	–30:05:57.80	16.58	1.904	1.96	1.3	4450	0.11	0.29	–
1	69	73472	18:04:22.33	–30:04:15.50	16.73	2.193	1.98	1.5	4400	0.49	0.48	–
0	70	64005	18:04:21.76	–30:06:12.00	16.58	1.959	1.99	1.4	4500	–0.25	0.19	–
0	71	205265	18:04:33.17	–30:09:49.70	16.45	2.155	1.94	1.3	4500	0.02	0.32	–
1	72	214042	18:04:29.19	–30:06:11.80	16.65	2.256	1.76	1.3	4150	0.38	0.39	–
0	73	350483	18:04:48.98	–30:08:07.20	16.83	2.511	1.87	1.3	4200	0.14	0.39	–
0	74	64018	18:04:22.49	–30:06:04.50	16.42	1.777	1.92	1.5	4500	0.15	0.33	–
0	75	63859	18:04:13.08	–30:05:10.80	16.43	1.931	1.86	1.5	4400	0.25	0.33	–
0	76	545445	18:04:06.17	–30:05:55.20	16.56	1.955	2.01	1.5	4550	0.13	0.29	–
0	77	63840	18:04:08.08	–30:06:19.40	16.59	1.950	1.99	1.1	4500	0.31	0.41	–
1	78	54108	18:04:11.63	–30:09:49.10	16.55	2.193	1.91	1.5	4400	0.46	0.42	–
1	79	54125	18:04:12.91	–30:09:05.60	16.77	2.335	2.00	1.3	4400	0.07	0.36	–
1	80	73467	18:04:08.39	–30:04:37.80	17.04	2.544	2.00	1.4	4250	0.12	0.35	–
1	81	54133	18:04:15.65	–30:08:53.50	16.64	2.156	1.67	1.0	4050	0.35	0.44	–
0	82	54078	18:04:22.03	–30:11:20.90	16.59	2.113	1.89	1.5	4350	0.09	0.35	–
2	83	63829	18:04:15.01	–30:07:08.60	16.79	2.231	2.01	1.5	4400	–0.01	0.40	–
0	85	537095	18:04:03.45	–30:09:57.60	16.45	1.824	1.93	1.2	4500	0.31	0.32	–
0	86	545222	18:03:57.53	–30:08:21.20	16.41	2.079	1.78	1.4	4300	0.16	0.36	–
0	87	545438	18:04:02.43	–30:06:05.60	16.80	2.147	1.97	1.5	4350	0.12	0.28	–
0	88	545233	18:03:59.73	–30:07:46.90	16.56	2.256	1.88	1.3	4350	0.31	0.41	–
2	91	545313	18:03:56.58	–30:08:06.00	16.90	2.289	2.05	1.4	4400	0.19	0.30	–
0	92	537092	18:04:06.28	–30:09:59.40	16.53	1.956	2.03	1.0	4600	–0.25	0.20	–
2	93	545277	18:04:05.34	–30:05:52.50	16.95	2.530	1.84	1.2	4100	0.35	0.46	–
1	95	402415	18:03:49.43	–30:04:39.30	16.65	2.042	2.08	1.2	4600	0.01	0.28	–
0	96	554670	18:03:56.05	–30:03:54.10	16.62	2.248	1.75	1.3	4150	–0.26	0.26	–
1	97	554748	18:03:55.84	–30:04:35.30	16.42	1.798	1.99	1.3	4600	0.39	0.49	–
0	98	392952	18:03:49.50	–30:05:28.30	16.61	2.196	1.79	1.5	4200	0.13	0.31	–
1	99	392896	18:03:41.61	–30:07:54.60	16.64	2.407	1.80	1.3	4200	–0.12	0.36	–
0	100	393083	18:03:49.11	–30:06:13.80	16.65	1.974	1.98	1.5	4450	0.03	0.25	–
0	101	393053	18:03:48.01	–30:06:51.10	16.63	2.009	1.83	1.2	4250	0.49	0.47	–
0	102	392931	18:03:51.84	–30:06:27.90	16.42	1.990	1.89	1.5	4450	–0.04	0.27	–
0	103	545269	18:03:53.81	–30:06:15.80	16.63	2.225	1.83	1.1	4250	0.45	0.40	–
0	104	554683	18:04:04.81	–30:03:00.00	16.61	2.032	2.00	1.2	4500	–0.20	0.25	–
0	105	554668	18:04:00.27	–30:04:00.60	16.58	2.157	1.85	1.3	4300	0.08	0.35	–
2	107	78106	18:03:19.96	–30:04:27.00	16.89	2.398	1.98	1.2	4300	–0.17	0.35	–
0	108	402498	18:03:40.67	–30:03:27.80	16.46	1.857	1.90	1.2	4450	0.55	0.42	–
1	109	234704	18:03:25.02	–30:05:01.50	16.42	1.936	1.93	1.4	4500	–0.18	0.28	–
0	110	67494	18:03:16.82	–30:06:10.80	16.43	1.959	2.02	1.1	4650	–0.05	0.25	–
0	111	234701	18:03:33.22	–30:05:08.40	16.56	2.027	1.98	1.2	4500	0.12	0.38	–

Table 3. continued.

QF[a]	ID	OGLE-ID	RA	Dec	V	$V-I$	$\log g$	V_t	$T_{\rm eff}$	[Fe/H]	σ^b	Cluster?
1	112	234888	18:03:32.84	–30:05:44.60	17.00	2.384	1.94	1.5	4200	0.28	0.45	–
1	113	554713	18:03:56.58	–30:01:55.50	16.81	2.387	1.90	1.4	4250	0.20	0.41	–
0	114	554956	18:04:01.61	–30:01:49.20	16.43	1.954	1.99	1.1	4600	–0.01	0.27	–
1	115	392951	18:03:42.68	–30:05:29.80	16.63	2.010	2.10	1.3	4650	0.10	0.34	–
0	116	412750	18:03:39.50	–30:00:53.80	16.45	1.946	1.83	1.1	4350	0.11	0.28	–
0	117	411479	18:03:36.82	–30:01:46.90	16.43	1.919	2.32	1.2	5200	–0.30	0.18	–
0	118	402656	18:03:38.71	–30:01:30.20	16.42	1.805	2.08	1.2	4750	–0.32	0.25	–
1	119	554694	18:04:04.57	–30:02:39.60	16.69	2.446	1.89	1.2	4300	0.15	0.47	–
0	120	402375	18:03:45.77	–30:02:02.30	16.65	2.228	1.80	1.4	4200	0.05	0.35	–
0	121	244829	18:03:36.41	–30:02:19.80	16.40	1.724	2.09	1.4	4800	–1.09	0.18	NGC 6522
2	122	402353	18:03:42.24	–30:02:38.80	16.84	2.624	2.27	1.5	4800	0.01	0.42	–
0	123	244738	18:03:27.62	–30:03:11.40	16.45	1.788	2.12	1.3	4800	–0.25	0.22	–
0	124	402347	18:03:44.54	–30:02:52.90	16.71	2.395	1.82	1.2	4200	0.19	0.45	–
0	126	564772	18:03:53.92	–29:59:44.20	16.75	2.542	1.92	1.5	4300	–0.07	0.44	–
1	128	423286	18:03:40.01	–29:57:54.80	16.62	2.130	1.90	1.2	4350	0.05	0.33	–
0	129	267974	18:03:24.89	–29:55:55.10	16.63	2.057	1.94	1.2	4400	0.31	0.39	–
0	133	412753	18:03:52.50	–30:00:50.90	16.57	2.136	1.84	1.1	4300	0.33	0.35	–
1	134	256345	18:03:23.54	–29:58:29.50	16.50	2.057	1.78	1.5	4250	0.33	0.44	–
Field at $b = -6°$												
0	2	41958c3	18:10:11.78	–31:39:03.30	15.64	1.506	2.04	1.5	5100	0.05	0.19	–
0	3	157820c3	18:10:04.89	–31:36:45.30	15.63	1.588	1.87	1.6	4800	–0.73	0.13	–
0	4	32799c3	18:10:09.69	–31:40:21.90	15.99	1.546	2.04	1.5	4850	–1.25	0.19	–
0	5	76187c3	18:09:56.25	–31:34:12.70	15.79	1.771	1.79	1.6	4550	–0.42	0.16	–
0	6	38354c3	18:10:04.92	–31:39:34.00	15.67	1.671	1.83	1.7	4700	–0.61	0.13	–
0	7	203158c3	18:10:14.94	–31:40:51.40	15.58	1.578	1.86	1.6	4800	–0.04	0.13	–
0	8	39802c3	18:10:00.70	–31:39:21.50	15.85	1.413	2.17	1.6	5200	–0.50	0.16	–
0	9	43054c3	18:10:01.23	–31:38:53.50	15.98	1.542	2.01	1.5	4800	–1.03	0.15	–
0	10	46885c3	18:09:55.24	–31:38:21.40	15.89	1.843	1.70	1.5	4350	0.00	0.18	–
0	11	1604c2	18:10:19.01	–31:44:50.60	15.90	1.627	1.92	1.4	4700	–1.13	0.16	NGC 6558
0	12	36989c3	18:09:54.14	–31:39:46.00	15.78	1.658	1.88	1.5	4700	0.05	0.17	–
0	13	36067c3	18:09:53.51	–31:39:53.70	15.77	1.731	1.78	1.4	4550	0.08	0.21	–
0	15	77454c2	18:10:24.40	–31:33:39.80	15.60	1.557	1.95	1.6	4950	–0.38	0.13	–
0	16	43562c2	18:10:20.85	–31:38:37.90	15.84	1.702	1.84	1.7	4600	–0.81	0.14	–
0	17	32832c2	18:10:18.07	–31:40:13.80	15.92	1.777	1.71	1.5	4350	–0.03	0.19	–
0	18	62009c2	18:10:16.95	–31:35:55.30	15.96	1.734	1.73	1.5	4350	–0.39	0.11	–
0	19	38565c2	18:10:15.97	–31:39:22.80	15.90	1.723	1.87	1.7	4600	–0.26	0.11	–
0	20	204270c3	18:10:14.79	–31:39:30.30	15.93	1.571	2.05	1.3	4900	0.02	0.13	–
0	21	69429c3	18:10:10.00	–31:35:09.60	15.86	1.747	1.79	1.5	4500	–0.76	0.12	–
0	22	56671c3	18:10:10.33	–31:36:57.50	15.76	1.576	1.98	1.3	4900	–0.20	0.12	–
0	23	25213c2	18:10:31.18	–31:41:20.60	15.92	1.604	1.87	1.5	4600	0.09	0.17	–
0	24	35428c2	18:10:33.48	–31:39:51.20	15.76	1.506	1.92	1.6	4800	–1.16	0.17	–
0	26	31338c2	18:10:29.03	–31:40:27.20	15.80	1.669	1.89	1.6	4700	–0.55	0.14	–
0	28	53477c2	18:10:32.42	–31:37:09.60	15.77	1.686	1.85	1.6	4650	–0.55	0.14	–
0	29	56410c2	18:10:30.35	–31:36:44.00	15.77	1.680	1.81	1.5	4600	–1.10	0.13	–
0	30	4799c2	18:10:20.10	–31:44:21.90	15.98	1.521	2.10	1.2	4950	–0.12	0.13	–
2	31	43239c2	18:10:25.53	–31:38:40.80	15.93	1.459	2.19	1.6	5200	–1.26	0.16	–
0	33	14297c2	18:10:50.22	–31:42:57.00	15.84	1.516	2.01	1.8	4900	–0.66	0.13	–
0	34	17437c2	18:10:41.67	–31:42:29.20	15.87	1.616	1.97	1.6	4800	–0.50	0.13	–
1	35	41995c2	18:10:45.45	–31:38:51.60	15.91	1.533	1.98	2.0	4800	–1.58	0.16	–
0	36	30173c2	18:10:35.61	–31:40:37.30	15.93	1.483	2.05	1.7	4900	–0.90	0.18	–
0	37	45160c2	18:10:52.14	–31:38:23.20	15.87	1.722	1.91	1.5	4700	–0.56	0.12	–
0	38	13661c2	18:10:35.13	–31:43:02.70	15.81	1.546	1.98	1.5	4850	–0.09	0.11	–
0	39	212324c6	18:10:26.03	–31:45:13.20	15.65	1.548	1.88	1.2	4800	–0.32	0.18	–
0	40	10381c2	18:10:27.82	–31:43:32.10	15.84	1.552	1.90	1.3	4700	–0.14	0.16	–
0	41	14893c2	18:10:42.48	–31:42:51.80	15.99	1.870	1.51	1.5	4050	–0.47	0.16	–
0	42	204828c2	18:10:53.24	–31:38:26.70	15.91	1.539	2.10	1.5	5000	–0.22	0.15	–
0	43	203913c2	18:10:54.62	–31:39:38.00	15.63	1.550	1.93	1.5	4900	–0.24	0.12	–
0	44	33058c2	18:10:41.51	–31:40:11.80	15.90	1.732	1.84	1.7	4550	–0.35	0.17	–
0	45	212175c6	18:10:53.08	–31:45:21.60	15.90	1.779	1.90	1.5	4650	–0.47	0.14	–
0	46	213150c6	18:10:47.52	–31:45:05.30	15.92	1.895	1.67	1.5	4300	–0.02	0.17	–
0	48	1678c2	18:10:40.43	–31:44:49.80	15.76	1.512	1.98	1.8	4900	–0.95	0.13	–
0	49	874c2	18:10:45.83	–31:44:56.60	15.91	1.772	1.84	1.5	4550	–0.32	0.13	–
0	50	7694c2	18:10:50.37	–31:43:55.60	15.80	1.434	2.11	1.9	5100	0.15	0.19	–

Table 3. continued.

QF[a]	ID	OGLE-ID	RA	Dec	V	$V-I$	$\log g$	V_t	$T_{\rm eff}$	[Fe/H]	σ^b	Cluster?
0	51	8312c2	18:10:39.22	–31:43:50.30	15.85	1.511	2.07	2.0	5000	–0.32	0.13	–
0	52	19402c1	18:11:13.14	–31:42:05.50	15.87	1.739	1.83	1.5	4550	–0.61	0.13	–
0	53	23483c1	18:11:08.20	–31:41:28.70	15.51	1.411	2.01	1.4	5150	–0.52	0.12	–
0	54	98692c6	18:10:15.50	–31:46:54.00	15.99	1.498	2.22	1.4	5000	0.07	0.18	–
0	55	94324c6	18:10:37.62	–31:47:33.00	15.82	1.736	1.90	1.6	4700	–0.39	0.13	–
0	56	99147c5	18:11:07.80	–31:46:29.00	15.96	1.742	1.86	1.6	4550	–0.60	0.14	–
0	58	96158c6	18:10:45.14	–31:47:16.80	15.92	1.610	2.10	1.4	5000	–0.37	0.17	–
0	60	100047c6	18:10:52.30	–31:46:42.10	15.95	1.891	1.72	1.5	4350	–0.33	0.14	–
0	61	102180c6	18:10:36.37	–31:46:23.50	15.95	1.782	1.86	1.4	4550	–0.39	0.14	–
0	62	211484c6	18:10:53.63	–31:46:31.10	15.75	1.683	1.92	1.4	4800	–0.60	0.11	–
0	64	106969c6	18:10:18.03	–31:45:43.50	15.70	1.473	1.98	1.5	4950	–1.00	0.19	NGC 6558
0	65	91438c6	18:10:17.39	–31:47:58.40	15.73	1.447	2.10	1.4	5150	–0.62	0.12	–
0	66	74262c6	18:10:50.66	–31:50:30.70	15.93	1.542	2.08	1.2	4950	–0.32	0.16	–
0	67	79869c6	18:10:31.64	–31:49:40.90	15.88	1.495	2.23	1.4	5300	–0.48	0.15	–
0	69	98974c6	18:10:36.36	–31:46:51.60	15.72	1.469	2.12	1.3	5200	–0.39	0.18	–
0	70	99069c6	18:10:22.08	–31:46:50.70	15.86	1.418	2.27	1.6	5400	–0.26	0.20	–
0	72	100384c6	18:10:25.39	–31:46:39.10	15.89	1.673	1.83	1.6	4550	–0.57	0.12	–
0	73	108928c6	18:10:21.50	–31:45:26.70	15.79	1.552	1.96	1.5	4850	–0.88	0.15	NGC 6558
0	74	101274c6	18:10:27.26	–31:46:31.50	15.83	1.486	2.14	1.5	5150	–0.06	0.11	–
0	75	71769c6	18:10:32.70	–31:50:52.80	15.62	1.442	2.13	1.5	5300	–0.22	0.19	–
0	77	62520c6	18:10:21.66	–31:52:14.40	15.98	1.491	2.09	1.5	4950	–0.84	0.19	–
0	78	60577c6	18:10:24.24	–31:52:31.50	15.73	1.573	1.97	1.5	4900	–0.18	0.16	–
0	79	43679c6	18:10:28.35	–31:55:00.70	15.99	1.510	2.10	1.4	4950	–0.59	0.18	–
0	80	55804c6	18:10:27.09	–31:53:14.00	15.99	1.854	1.54	1.5	4100	0.19	0.24	–
0	81	54561c6	18:10:29.53	–31:53:24.70	15.73	1.442	1.97	1.4	4900	–0.25	0.13	–
0	82	80281c6	18:10:22.17	–31:49:37.30	15.98	1.490	2.15	1.5	5050	–0.08	0.11	–
0	83	68782c6	18:10:30.71	–31:51:18.90	15.83	1.718	1.93	1.5	4750	–0.50	0.16	–
0	84	66376c6	18:10:32.44	–31:51:40.50	15.82	1.536	1.87	1.5	4650	0.19	0.20	–
0	85	205837c7	18:10:15.10	–31:54:11.20	15.89	1.701	1.95	1.6	4750	–0.36	0.13	–
0	87	75097c7	18:10:12.85	–31:50:30.60	15.87	1.722	1.82	1.5	4550	–0.09	0.17	–
0	88	63747c7	18:10:10.96	–31:52:10.40	15.77	1.560	2.02	1.5	4950	–0.09	0.16	–
0	90	46642c7	18:10:01.82	–31:54:39.00	15.94	1.599	1.91	1.5	4650	0.21	0.24	–
0	91	57883c7	18:10:05.62	–31:53:01.40	15.84	1.815	1.81	1.5	4550	–0.25	0.16	–
0	92	51688c6	18:10:17.72	–31:53:50.10	15.96	1.721	1.95	1.5	4700	–0.42	0.15	–
0	93	209695c7	18:10:14.80	–31:49:31.70	15.97	1.556	2.07	1.4	4900	–0.11	0.12	–
0	95	90337c7	18:10:11.51	–31:48:19.20	15.91	1.824	2.02	1.5	4850	–0.27	0.20	–
0	99	87232c7	18:10:04.39	–31:48:45.80	15.81	1.476	2.03	1.5	4950	–0.21	0.12	–
0	100	54480c7	18:09:46.34	–31:53:30.30	15.74	1.473	2.08	1.5	5100	–0.40	0.12	–
0	102	64860c7	18:09:56.69	–31:52:00.40	15.88	1.715	1.80	1.5	4500	0.09	0.20	–
0	103	79003c7	18:10:04.43	–31:49:56.80	15.62	1.474	2.08	1.5	5200	–0.40	0.13	–
0	104	50439c7	18:09:56.09	–31:54:06.20	15.93	1.508	2.16	1.4	5100	–0.08	0.18	–
0	105	80144c7	18:10:07.44	–31:49:47.10	15.58	1.556	1.83	1.5	4750	–0.05	0.13	–
0	107	97618c7	18:09:39.57	–31:47:15.80	15.51	1.512	1.88	1.5	4900	–0.91	0.17	–
0	108	102010c7	18:09:54.38	–31:46:37.60	15.77	1.606	1.90	1.4	4750	–0.56	0.12	–
0	109	87242c8	18:09:26.69	–31:48:58.50	15.92	1.899	1.67	1.5	4300	0.00	0.24	–
0	111	88768c7	18:09:43.40	–31:48:32.30	15.86	1.711	1.72	1.5	4400	–0.25	0.14	–
0	112	86105c7	18:09:44.61	–31:48:55.00	15.94	1.621	2.06	1.4	4900	–0.14	0.14	–
0	113	77209c7	18:09:36.36	–31:50:12.00	15.90	1.536	1.98	1.3	4800	–0.43	0.14	–
0	114	98458c7	18:10:01.97	–31:47:08.40	15.93	1.846	1.68	1.5	4300	–0.02	0.16	–
1	116	5685c3	18:09:52.41	–31:44:13.30	15.78	1.554	1.98	1.5	4900	–1.15	0.16	–
2	117	104943c6	18:10:16.42	–31:46:00.50	15.60	1.442	2.10	1.5	5300	–1.20	0.16	NGC 6558
0	118	5118c4	18:09:25.84	–31:44:15.60	15.89	1.588	1.95	1.6	4750	0.06	0.17	–
0	119	110465c7	18:10:07.79	–31:45:25.10	15.99	1.716	1.90	1.4	4600	0.00	0.21	–
0	120	212654c8	18:09:33.44	–31:45:25.00	15.89	1.556	2.01	1.4	4850	0.39	0.26	–
0	121	108191c7	18:09:45.55	–31:45:44.60	15.90	1.454	2.11	1.5	5050	–0.77	0.11	–
0	122	23017c3	18:10:04.46	–31:41:45.30	15.96	1.941	1.65	1.5	4250	0.09	0.21	–
0	123	101167c8	18:09:20.54	–31:47:00.20	15.92	1.496	2.16	1.5	5100	0.05	0.13	–
0	124	103592c7	18:09:50.04	–31:46:23.70	15.85	1.624	1.99	1.5	4850	–0.31	0.18	–
0	126	202633c3	18:10:13.06	–31:41:28.50	15.71	1.655	1.73	1.5	4500	0.31	0.26	–
0	127	32080c3	18:09:51.13	–31:40:28.00	15.63	1.549	1.99	1.6	5000	–0.17	0.13	–
0	128	43791c3	18:09:37.90	–31:38:46.50	15.71	1.534	2.20	1.3	4950	0.00	0.15	–
0	129	204664c4	18:09:34.75	–31:38:50.90	15.72	1.478	2.22	1.5	5400	0.18	0.12	–
1	132	11653c3	18:09:56.84	–31:43:22.50	15.65	1.613	1.91	1.5	4850	0.13	0.22	–

Table 3. continued.

QF[a]	ID	OGLE-ID	RA	Dec	V	$V-I$	$\log g$	V_t	$T_{\rm eff}$	[Fe/H]	σ^b	Cluster?
0	134	21259c2	18:10:17.72	–31:41:55.20	15.71	1.545	2.02	1.5	5000	–0.08	0.14	–
0	3	200810c3	18:10:13.35	–31:43:37.70	16.28	2.117	1.66	1.5	4100	0.11	0.19	–
0	5	34058c3	18:10:04.37	–31:40:10.90	16.16	1.686	1.84	1.6	4400	0.21	0.19	–
0	6	47752c3	18:09:59.53	–31:38:14.10	16.31	1.940	1.47	1.5	3900	0.20	0.20	–
0	8	40528c3	18:09:58.10	–31:39:15.20	16.17	1.850	1.88	1.7	4450	–0.48	0.14	–
0	10	29280c3	18:09:50.48	–31:40:51.60	16.15	1.855	1.80	1.5	4350	0.18	0.20	–
2	11	12982c3	18:10:07.98	–31:43:11.20	16.61	2.426	1.95	1.5	4300	0.01	0.50	–
0	13	108051c7	18:09:55.95	–31:45:46.30	16.29	2.107	1.79	1.6	4250	–0.09	0.21	–
0	15	20863c2	18:10:22.73	–31:41:58.80	16.30	2.006	1.75	1.5	4200	0.08	0.23	–
0	16	31220c2	18:10:19.06	–31:40:28.10	16.09	1.615	1.81	1.7	4400	–0.02	0.17	–
1	17	50086c2	18:10:15.56	–31:37:40.00	16.15	1.804	1.80	1.5	4350	0.32	0.26	–
0	18	208608c3	18:10:14.06	–31:33:52.00	16.17	1.751	2.06	1.5	4750	–0.56	0.13	–
0	20	58159c3	18:10:08.82	–31:36:44.50	16.38	1.895	1.93	1.5	4400	–0.09	0.15	–
2	21	70770c3	18:10:06.95	–31:34:58.40	16.27	1.949	1.61	1.5	4050	–0.04	0.31	–
0	23	205096c2	18:10:39.82	–31:38:06.90	16.18	1.792	2.10	1.4	4800	–0.15	0.12	–
0	24	148090c2	18:10:32.27	–31:39:15.10	16.20	1.767	2.05	1.5	4700	–0.28	0.16	–
0	25	42348c2	18:10:32.46	–31:38:48.90	16.16	1.785	1.84	1.5	4400	–0.09	0.15	–
0	27	149531c2	18:10:27.61	–31:38:49.70	16.15	1.810	1.91	1.5	4500	–0.38	0.12	–
0	28	31090c2	18:10:37.38	–31:40:29.10	16.04	1.671	1.98	1.5	4700	–0.26	0.11	–
1	29	14261c2	18:10:16.93	–31:42:57.50	16.23	1.838	1.72	1.4	4200	0.40	0.24	–
0	30	69986c2	18:10:28.56	–31:34:46.20	16.19	1.781	2.01	1.5	4650	–0.27	0.14	–
1	31	73344c2	18:10:27.05	–31:34:15.80	16.52	2.252	2.05	1.5	4500	–0.00	0.30	–
1	34	139560c2	18:10:45.15	–31:41:57.90	16.42	2.040	1.87	1.5	4300	0.26	0.33	–
2	35	145595c2	18:10:39.53	–31:39:58.90	16.27	2.169	1.81	1.5	4300	0.44	0.39	–
0	36	22905c2	18:10:28.24	–31:41:40.70	16.10	1.673	1.89	1.4	4500	–0.45	0.12	–
0	37	47298c2	18:10:49.67	–31:38:04.10	16.10	1.853	1.79	1.7	4350	–0.51	0.12	–
1	38	33601c1	18:10:56.00	–31:39:56.60	16.42	2.059	1.94	1.6	4400	0.29	0.27	–
0	39	43023c2	18:10:38.81	–31:38:42.60	16.10	1.718	1.95	1.4	4600	–0.46	0.16	–
2	42	107527c6	18:10:17.65	–31:45:38.90	16.05	1.612	1.20	1.5	3750	–0.96	0.18	NGC 6558
0	43	31176c2	18:10:44.56	–31:40:28.40	16.01	1.875	1.76	1.5	4400	–0.22	0.13	–
0	44	17038c2	18:10:36.15	–31:42:32.70	16.14	1.748	1.76	1.4	4300	0.29	0.22	–
1	45	103742c5	18:10:58.15	–31:45:48.00	16.37	1.929	1.69	1.5	4100	0.31	0.19	–
0	49	959c2	18:10:33.83	–31:44:56.10	16.16	1.686	2.00	1.4	4650	–0.58	0.12	–
0	51	10584c2	18:10:47.85	–31:43:29.80	16.17	1.751	1.91	1.4	4500	–0.38	0.13	–
0	52	15094c1	18:10:55.31	–31:42:44.40	16.25	1.797	2.01	1.4	4600	–0.19	0.15	–
0	54	95371c6	18:10:34.70	–31:47:23.70	16.20	1.817	1.92	1.4	4500	–0.27	0.15	–
0	55	98734c6	18:10:28.14	–31:46:53.60	16.06	1.654	1.99	1.1	4700	–0.06	0.17	–
0	56	103413c6	18:10:52.64	–31:46:13.00	16.16	1.798	1.65	1.4	4150	0.24	0.25	–
0	57	85625c5	18:10:57.19	–31:48:26.30	16.39	2.224	1.82	1.5	4250	0.15	0.23	–
0	58	91631c6	18:10:44.26	–31:47:56.80	16.07	1.608	2.05	1.5	4800	–0.28	0.15	–
0	59	95545c6	18:10:49.00	–31:47:22.00	16.25	1.892	1.77	1.3	4250	–0.45	0.12	–
1	61	96460c6	18:10:50.03	–31:47:14.00	16.01	1.685	1.94	1.4	4650	0.25	0.21	–
1	62	83500c6	18:10:33.98	–31:49:09.10	16.40	2.172	2.00	1.4	4400	0.09	0.30	–
0	64	72513c6	18:10:43.80	–31:50:46.30	16.04	1.624	1.98	1.7	4700	–0.48	0.16	–
0	65	69731c6	18:10:35.15	–31:51:10.60	16.34	1.913	1.95	1.5	4450	–0.19	0.19	–
1	66	73072c6	18:10:49.86	–31:50:41.50	16.25	2.132	1.60	1.5	4050	0.12	0.28	–
0	68	56641c6	18:10:38.77	–31:53:06.90	16.00	1.675	1.81	1.5	4450	0.17	0.20	–
0	69	208907c6	18:10:53.38	–31:50:12.50	16.03	1.581	2.09	1.5	4900	–0.17	0.15	–
0	70	99166c6	18:10:23.01	–31:46:49.60	16.26	1.894	1.81	1.4	4300	0.04	0.23	–
0	71	71832c6	18:10:29.83	–31:50:52.30	16.24	1.963	1.80	1.4	4300	–0.09	0.19	–
0	72	77481c6	18:10:43.18	–31:50:02.10	16.05	1.555	2.13	1.5	4950	–0.28	0.09	–
0	73	91776c6	18:10:32.31	–31:47:55.50	16.20	1.751	2.11	1.5	4800	0.23	0.24	–
0	74	93621c6	18:10:24.21	–31:47:39.30	16.11	1.727	1.92	1.5	4550	–0.22	0.17	–
0	75	99940c6	18:10:15.34	–31:46:43.10	16.13	1.771	1.69	1.6	4200	–0.25	0.12	–
0	78	53554c6	18:10:20.77	–31:53:33.40	16.10	1.910	1.78	1.4	4350	0.08	0.21	–
0	79	63690c6	18:10:22.57	–31:52:04.20	16.08	1.607	2.06	1.5	4800	0.03	0.16	–
0	80	205097c6	18:10:26.99	–31:54:51.70	16.54	2.279	2.18	1.4	4700	0.26	0.21	–
0	81	52922c6	18:10:27.94	–31:53:39.10	16.24	1.753	1.94	1.5	4500	–0.30	0.14	–
0	82	51954c6	18:10:29.15	–31:53:47.60	16.14	1.756	1.76	1.5	4300	0.03	0.22	–
0	83	56533c6	18:10:32.58	–31:53:07.70	16.05	1.670	1.72	1.5	4300	0.13	0.30	–
0	84	94909c7	18:10:12.67	–31:47:39.80	16.14	2.112	1.73	1.4	4250	–0.11	0.26	–
0	85	73484c7	18:10:12.00	–31:50:44.70	16.40	1.988	2.07	1.2	4600	0.31	0.25	–
0	86	90995c7	18:10:09.65	–31:48:13.70	16.11	1.619	2.07	1.4	4800	–0.03	0.18	–

Table 3. continued.

QF[a]	ID	OGLE-ID	RA	Dec	V	$V-I$	$\log g$	V_t	$T_{\rm eff}$	[Fe/H]	σ^b	Cluster?
0	87	41505c7	18:10:07.59	–31:55:23.30	16.09	1.670	2.06	1.6	4800	–0.48	0.15	–
1	88	34034c7	18:10:03.84	–31:56:28.90	16.33	2.064	1.87	1.5	4350	0.04	0.24	–
1	89	205852c7	18:10:13.63	–31:54:09.60	16.30	1.797	1.86	1.5	4350	0.06	0.31	–
1	90	64944c7	18:10:02.47	–31:51:59.80	16.20	2.088	1.79	1.5	4350	0.08	0.23	–
0	91	75601c7	18:10:09.16	–31:50:26.30	16.03	1.891	1.79	1.5	4400	–0.08	0.28	–
0	92	60208c7	18:10:07.77	–31:52:41.30	16.12	1.722	1.83	1.6	4400	–0.37	0.09	–
0	93	46088c7	18:10:08.96	–31:54:43.70	16.14	1.869	1.90	1.4	4500	–0.20	0.16	–
1	95	77743c7	18:09:49.10	–31:50:07.60	16.09	1.703	1.78	1.5	4350	0.25	0.22	–
0	96	85832c7	18:09:52.99	–31:48:57.70	16.25	1.884	1.77	1.5	4250	0.01	0.20	–
2	97	211927c7	18:10:15.21	–31:46:00.60	16.04	1.620	2.06	1.0	4850	–0.81	0.24	NGC 6558
1	98	93881c7	18:10:02.82	–31:47:48.50	16.13	1.882	1.83	1.5	4400	0.03	0.25	–
0	99	82739c7	18:09:58.42	–31:49:24.60	16.20	1.781	1.99	1.5	4600	–0.45	0.14	–
0	100	88860c7	18:10:03.71	–31:48:31.80	16.09	1.884	1.85	1.5	4450	–0.06	0.20	–
0	101	62874c7	18:09:51.36	–31:52:17.70	16.03	1.820	1.92	1.5	4600	–0.48	0.17	–
0	102	73636c7	18:09:56.93	–31:50:43.20	16.11	1.686	1.86	1.5	4450	–0.22	0.12	–
0	103	56730c7	18:09:53.17	–31:53:10.80	16.31	1.980	1.83	1.3	4300	0.00	0.21	–
0	104	48678c7	18:09:52.26	–31:54:21.10	16.02	1.622	2.00	1.6	4750	0.17	0.24	–
0	105	58592c7	18:09:57.44	–31:52:55.10	16.20	1.908	1.95	1.6	4550	0.17	0.22	–
0	106	77419c7	18:10:04.15	–31:50:11.00	16.05	1.615	1.93	1.5	4600	0.18	0.21	–
1	107	96001c8	18:09:28.48	–31:47:44.30	16.05	1.603	1.89	1.5	4550	0.21	0.26	–
0	108	97453c7	18:09:39.52	–31:47:17.50	16.07	1.580	2.00	1.5	4700	0.02	0.17	–
0	109	105594c7	18:10:01.14	–31:46:06.90	16.06	1.591	2.10	1.6	4900	–0.25	0.11	–
1	110	80262c8	18:09:20.06	–31:49:58.20	16.22	1.766	2.06	1.5	4700	0.23	0.23	–
0	111	80419c8	18:09:26.94	–31:49:57.00	16.08	1.767	1.81	1.5	4400	0.18	0.24	–
1	112	98090c7	18:09:53.69	–31:47:11.80	16.01	1.766	1.88	1.6	4550	–0.05	0.34	–
0	113	75382c8	18:09:31.58	–31:50:39.60	16.18	1.748	1.88	1.5	4450	0.20	0.24	–
0	114	94445c7	18:09:57.05	–31:47:43.40	16.14	1.740	1.93	1.5	4550	–0.29	0.12	–
0	115	97069c7	18:10:02.43	–31:47:21.10	16.16	2.120	1.61	1.5	4100	0.25	0.48	–
2	116	132843c3	18:09:46.60	–31:44:16.00	16.15	2.019	2.00	1.5	4650	–0.05	0.55	–
0	117	8683c4	18:09:19.59	–31:43:43.60	16.05	1.907	1.69	1.4	4250	0.02	0.18	–
0	118	215027c7	18:10:05.98	–31:44:49.20	16.35	1.872	1.68	1.5	4100	0.20	0.24	–
0	119	213817c7	18:10:03.06	–31:45:00.90	16.13	1.687	1.86	1.5	4450	0.27	0.26	–
0	120	110776c7	18:09:45.13	–31:45:22.40	15.82	1.610	1.84	1.5	4600	–0.85	0.15	–
0	121	111007c8	18:09:27.43	–31:45:37.90	16.26	1.835	1.81	1.4	4300	0.01	0.20	–
0	123	108627c7	18:10:04.95	–31:45:40.80	16.31	2.043	2.03	1.4	4600	0.02	0.29	–
0	124	97461c8	18:09:21.33	–31:47:31.60	16.01	1.702	1.97	1.5	4700	0.31	0.26	–
2	126	35429c3	18:09:47.59	–31:39:58.90	16.59	2.230	2.01	1.5	4400	0.30	0.30	–
0	128	19346c3	18:09:55.66	–31:42:16.50	16.02	1.560	2.09	1.5	4900	0.27	0.15	–
0	129	41112c4	18:09:31.59	–31:39:07.50	16.10	1.719	1.89	1.5	4500	–0.31	0.13	–
0	130	9081c3	18:10:01.92	–31:43:44.80	16.22	1.782	1.93	1.5	4500	–0.25	0.15	–
0	131	35643c4	18:09:29.06	–31:39:54.20	16.01	1.522	2.17	1.6	5050	0.22	0.17	–
0	134	27350c4	18:09:23.23	–31:41:03.90	16.07	1.595	2.08	1.3	4850	–0.36	0.19	–
0	135	6693c3	18:09:55.37	–31:44:04.70	16.17	1.675	2.01	1.5	4650	–0.03	0.16	–
Field at $b = -12°$												
0	3	2002C3	18:35:06.73	–34:31:59.59	15.57	1.250	2.31	1.2	5000	–0.36	0.17	–
0	4	2374C3	18:35:08.04	–34:31:13.37	15.76	1.244	2.38	1.6	5000	–0.58	0.15	–
0	5	3142C3	18:35:09.48	–34:29:28.15	15.95	1.287	2.41	1.4	4900	–0.15	0.16	–
0	6	2947C3	18:35:00.59	–34:29:55.64	16.02	1.204	2.51	1.2	5050	–0.44	0.16	–
0	7	2200C3	18:34:57.77	–34:31:35.91	16.15	1.315	2.43	1.5	4800	–0.17	0.14	–
0	9	3018C3	18:35:03.59	–34:29:45.23	15.49	1.404	2.08	1.4	4650	–0.61	0.12	–
0	10	3515C5	18:34:50.72	–34:28:37.94	15.18	1.355	2.04	1.6	4800	0.00	0.16	–
0	11	2769C3	18:34:57.52	–34:30:21.29	15.78	1.295	2.45	1.5	5100	0.18	0.17	–
2	12	3109C3	18:34:45.67	–34:29:31.70	15.81	1.341	2.35	1.3	4900	–0.58	0.26	–
2	13	201583C3	18:34:51.39	–34:31:40.37	15.79	1.258	2.36	1.4	4950	–1.18	0.18	–
0	15	2470C3	18:35:21.52	–34:31:01.85	16.25	1.375	2.47	1.5	4800	–0.06	0.16	–
0	16	3267C3	18:35:22.06	–34:29:11.16	15.07	1.349	2.03	1.2	4850	0.01	0.14	–
0	17	3161C3	18:35:19.42	–34:29:26.65	15.46	1.306	2.27	1.6	5000	–0.12	0.12	–
0	19	4365C3	18:35:21.17	–34:26:50.97	16.08	1.148	2.53	1.6	5050	–0.66	0.15	–
0	20	6549C6	18:35:03.43	–34:37:24.28	15.70	1.320	2.31	1.3	4900	0.11	0.15	–
0	21	3733C3	18:35:17.99	–34:28:09.31	15.10	1.423	1.98	1.4	4750	–0.19	0.12	–
0	22	4085C3	18:35:13.57	–34:27:23.97	16.13	1.513	2.31	1.3	4600	–0.38	0.13	–
0	24	2525C2	18:35:46.60	–34:30:20.41	15.99	1.214	2.48	1.4	5000	–0.33	0.12	–
0	28	6505C6	18:35:18.68	–34:37:30.83	16.04	1.232	2.50	1.4	5000	–0.37	0.14	–

Table 3. continued.

QF[a]	ID	OGLE-ID	RA	Dec	V	$V-I$	$\log g$	V_t	$T_{\rm eff}$	[Fe/H]	σ^b	Cluster?
0	29	867C3	18:35:09.10	–34:34:34.73	15.76	1.228	2.38	1.4	5000	–0.46	0.12	–
0	31	222C3	18:35:14.90	–34:36:00.45	15.50	1.295	2.23	1.6	4900	–0.38	0.12	–
0	33	650C2	18:35:56.80	–34:34:48.25	15.29	1.530	1.81	1.4	4350	–0.67	0.10	–
0	35	2296C2	18:35:51.98	–34:30:52.18	15.90	1.223	2.54	1.5	5200	0.03	0.14	–
0	36	1876C2	18:35:49.38	–34:31:56.10	15.86	1.106	2.54	1.4	5250	–0.86	0.13	–
0	37	2335C2	18:35:58.85	–34:30:46.05	15.81	1.270	2.26	1.2	4750	–0.84	0.15	–
0	38	1814C1	18:36:11.58	–34:32:05.99	15.85	1.427	2.22	1.3	4650	–0.39	0.12	–
2	40	2052C2	18:35:59.96	–34:31:27.23	15.42	1.145	2.27	1.5	5050	–0.94	0.30	–
0	41	1156C2	18:35:56.02	–34:33:36.40	15.93	1.534	1.95	1.1	4200	–0.36	0.13	–
0	42	2407C2	18:36:01.99	–34:30:36.77	15.49	1.173	2.25	1.5	4950	–0.70	0.12	–
0	43	1918C1	18:36:07.53	–34:31:51.05	15.83	1.248	2.36	1.4	4900	–0.36	0.15	–
0	44	1917C1	18:36:12.50	–34:31:51.47	16.22	1.426	2.31	1.4	4550	0.18	0.29	–
0	45	6080C8	18:36:20.59	–34:38:24.15	15.89	1.358	2.33	1.4	4800	0.11	0.26	–
0	46	6426C8	18:36:10.10	–34:37:32.99	15.79	1.280	2.34	1.2	4900	–0.39	0.15	–
0	47	6391C8	18:36:23.58	–34:37:37.81	15.28	1.140	2.21	1.3	5050	–0.59	0.13	–
0	48	6637C8	18:36:07.58	–34:37:02.88	16.07	1.296	2.40	1.5	4800	–0.26	0.14	–
0	50	431C2	18:35:53.60	–34:35:21.07	15.63	1.175	2.41	1.3	5150	–0.02	0.15	–
0	51	455C1	18:36:17.85	–34:35:21.06	15.67	1.174	2.32	1.4	4950	–0.57	0.15	–
0	52	6828C7	18:35:56.25	–34:36:54.38	16.09	1.360	2.26	1.4	4550	0.17	0.17	–
2	53	608C1	18:36:13.69	–34:34:55.95	15.13	1.133	2.16	1.2	5100	–1.66	0.19	–
0	56	5487C8	18:36:14.63	–34:39:56.70	16.16	1.339	2.49	1.5	4900	–0.27	0.14	–
0	57	4478C8	18:36:16.70	–34:42:25.80	15.79	1.260	2.34	1.4	4900	–0.28	0.14	–
0	59	4740C8	18:36:19.30	–34:41:47.15	15.80	1.208	2.40	1.5	5000	–0.33	0.16	–
0	60	6913C7	18:35:52.67	–34:36:43.31	15.95	1.244	2.43	1.8	4950	–0.21	0.15	–
0	61	5351C8	18:36:08.00	–34:40:16.01	15.83	1.382	2.25	1.3	4700	–0.09	0.11	–
0	62	5400C8	18:36:12.37	–34:40:07.75	15.96	1.113	2.54	1.4	5150	0.14	0.14	–
0	64	2812C8	18:36:09.28	–34:46:23.50	15.63	1.458	1.95	1.2	4350	–0.62	0.14	–
0	65	3805C7	18:35:28.05	–34:43:52.10	15.70	1.342	2.43	1.4	5150	–0.38	0.14	–
0	68	2772C7	18:35:48.07	–34:46:25.83	15.10	1.258	2.07	1.4	4900	–0.22	0.14	–
0	70	3191C7	18:35:55.61	–34:45:21.91	15.40	1.243	2.24	1.4	5000	–0.28	0.12	–
1	71	2476C7	18:35:59.67	–34:47:07.64	15.96	1.120	2.51	1.4	5100	–0.66	0.19	–
0	72	3091C8	18:36:08.87	–34:45:43.81	15.32	1.236	2.21	1.4	5000	–0.36	0.15	–
1	74	3711C7	18:35:41.05	–34:44:06.11	15.71	1.097	2.58	1.4	5450	–0.30	0.16	–
0	75	3035C7	18:35:51.36	–34:45:45.52	15.68	1.191	2.27	1.4	4850	–0.61	0.14	–
2	76	1614C7	18:35:28.16	–34:49:06.49	15.27	1.142	2.10	1.3	4850	–0.73	0.33	–
2	77	1140C7	18:35:31.64	–34:50:16.35	16.23	1.355	2.42	1.4	5600	0.60	0.23	–
0	78	1491C7	18:35:33.53	–34:49:23.93	15.80	1.419	2.23	1.4	4700	–0.19	0.17	–
0	79	2110C7	18:35:36.10	–34:47:56.62	15.59	1.405	2.21	1.4	4800	–0.09	0.17	–
0	80	2220C7	18:35:30.72	–34:47:42.70	15.62	1.233	2.43	1.7	5200	–0.05	0.14	–
1	81	1554C7	18:35:40.37	–34:49:16.14	15.11	1.166	2.22	1.4	5200	–0.39	0.14	–
0	82	2178C7	18:35:41.56	–34:47:48.85	15.77	1.371	2.10	1.5	4500	–0.02	0.17	–
0	83	2422C7	18:35:48.06	–34:47:15.63	15.89	1.481	2.01	1.2	4300	0.26	0.25	–
0	84	3101C7	18:35:37.13	–34:45:34.59	15.86	1.233	2.37	1.1	4900	–0.34	0.14	–
1	86	2580C6	18:35:15.24	–34:46:41.38	16.06	1.566	1.66	1.4	3850	0.42	0.27	–
0	87	3238C6	18:35:16.99	–34:44:59.64	15.73	1.322	2.32	1.1	4900	–0.17	0.15	–
1	89	1417C7	18:35:26.03	–34:49:34.46	15.58	1.172	2.39	1.3	5150	–0.31	0.24	–
0	90	2532C6	18:35:13.18	–34:46:48.45	15.71	1.345	2.17	1.4	4650	–0.13	0.18	–
0	91	2948C7	18:35:24.53	–34:46:01.16	15.53	1.679	1.83	1.1	4250	0.02	0.17	–
0	92	1589C7	18:35:30.62	–34:49:10.88	15.87	1.164	2.56	1.4	5250	0.11	0.18	–
2	93	3690C7	18:35:28.35	–34:44:08.73	14.97	1.208	2.00	1.5	4900	–1.40	0.18	–
0	95	3796C6	18:34:58.25	–34:43:44.19	15.53	1.454	2.01	1.4	4500	–0.83	0.13	–
0	96	3786C6	18:34:49.35	–34:43:45.09	15.90	1.444	2.33	1.5	4800	–0.28	0.21	–
0	97	3201C6	18:35:03.02	–34:45:05.51	15.47	1.211	2.35	1.1	5150	–0.05	0.16	–
1	98	4217C6	18:34:55.12	–34:42:46.34	15.78	1.461	2.10	1.3	4500	–0.39	0.15	–
1	99	4333C6	18:35:04.91	–34:42:31.72	15.99	1.228	2.48	1.4	5000	–0.16	0.20	–
0	100	6164C6	18:34:58.84	–34:38:17.52	15.25	1.265	2.21	1.5	5050	–0.17	0.14	–
0	101	3350C6	18:35:14.53	–34:44:44.95	15.27	1.120	2.29	1.5	5200	–0.19	0.17	–
0	102	4263C6	18:35:01.81	–34:42:40.62	15.87	1.329	2.43	1.3	5000	–0.18	0.13	–
0	103	3558C6	18:35:12.93	–34:44:17.26	16.03	1.341	2.38	1.5	4800	–0.02	0.15	–
0	104	6090C6	18:35:20.05	–34:38:28.85	16.15	1.479	2.11	1.2	4300	0.11	0.22	–
1	105	1419C6	18:34:59.16	–34:49:29.22	15.82	1.485	2.12	1.2	4500	0.02	0.20	–
1	106	5543C6	18:35:15.85	–34:39:49.56	16.07	1.459	2.08	1.3	4300	0.12	0.22	–
0	107	5908C6	18:34:48.00	–34:38:54.03	15.66	1.151	2.41	1.3	5150	–0.67	0.16	–

Table 3. continued.

QF[a]	ID	OGLE-ID	RA	Dec	V	$V-I$	$\log g$	V_t	$T_{\rm eff}$	[Fe/H]	σ^b	Cluster?
0	108	4876C6	18:35:12.29	–34:41:18.14	16.08	1.303	2.46	1.3	4900	–0.59	0.12	–
0	109	5319C6	18:34:43.24	–34:40:18.83	15.58	1.447	2.09	1.3	4600	–0.36	0.16	–
1	110	6263C6	18:35:14.21	–34:38:05.96	16.01	1.648	1.79	1.5	4000	0.64	0.38	–
0	111	5977C6	18:35:12.22	–34:38:45.31	15.31	1.334	2.01	1.7	4650	0.09	0.17	–
2	112	4612C6	18:35:01.15	–34:41:54.14	16.02	1.264	2.46	1.5	4950	–0.82	0.17	–
0	113	5588C6	18:35:06.42	–34:39:42.10	15.87	1.282	2.37	1.1	4900	–0.28	0.11	–
0	114	5664C6	18:34:52.60	–34:39:31.75	15.43	1.330	2.14	1.5	4800	0.15	0.19	–
0	115	3965C6	18:34:59.18	–34:43:22.14	15.46	1.663	1.91	1.5	4400	–0.20	0.14	–
0	116	159C4	18:34:30.32	–34:36:06.99	15.66	1.435	2.18	1.5	4700	–0.14	0.22	–
0	117	6717C6	18:34:52.39	–34:37:01.77	15.58	1.283	2.29	1.4	4950	–0.23	0.13	–
0	118	5980C6	18:34:43.98	–34:38:44.23	15.93	1.242	2.45	1.4	5000	–0.25	0.16	–
0	119	7119C5	18:34:32.34	–34:37:03.86	15.12	1.381	1.96	1.3	4700	–0.33	0.14	–
0	120	6419C5	18:34:30.96	–34:38:29.97	15.40	1.390	2.07	1.2	4700	–0.25	0.17	–
0	121	6230C5	18:34:33.98	–34:38:53.61	15.06	1.154	2.18	1.3	5150	0.09	0.16	–
2	122	6099C5	18:34:28.47	–34:39:11.53	15.72	1.288	2.34	1.3	4950	–0.78	0.30	–
2	123	5750C5	18:34:27.51	–34:39:55.71	15.56	1.130	2.35	1.4	5100	–0.29	0.30	–
0	124	5396C5	18:34:34.77	–34:40:42.70	15.63	1.282	2.20	1.5	4750	–0.16	0.22	–
1	126	2502C3	18:34:54.42	–34:30:56.51	15.97	1.330	2.44	1.4	4950	–0.39	0.15	–
0	128	1754C3	18:34:48.92	–34:32:32.69	15.43	1.301	2.23	1.3	4950	–0.20	0.12	–
0	129	1407C3	18:34:50.53	–34:33:22.68	15.76	1.155	2.35	1.0	4950	–0.82	0.20	–
1	132	1700C4	18:34:29.77	–34:32:44.84	15.67	1.288	2.35	1.4	5000	0.34	0.30	–
1	135	166C3	18:34:45.39	–34:36:07.17	15.90	1.267	2.30	1.5	4750	–0.86	0.24	–

[a] QF is a subjective quality factor, classifying stars into good (0), bad (2) and intermediate (1), according to how unique/degenerate the convergence into the final model atmosphere proceeded.
[b] Line-to-line dispersion around the mean [Fe/H].